Explosive Behavior of Intermediate Magmas: The Example of Cotopaxi Volcano (Ecuador)

Explosive behavior of intermediate magmas: the example of Cotopaxi volcano (Ecuador)

M. Pistolesi[1], A. Aravena[2,3], L. Costantini[4], C. Vigiani[2], R. Cioni[2], C. Bonadonna[4]

[1] Dipartimento di Scienze della Terra, Università di Pisa, Pisa, Italy

[2] Dipartimento di Scienze della Terra, Università di Firenze, Florence, Italy

[3] Laboratoire Magmas et Volcans, Université Clermont Auvergne, CNRS, IRD, OPGC, Clermont-Ferrand, France

[4] Département des Sciences de la Terre, Université de Genève, Geneva, Switzerland

Keypoints

- Five eruptions occurred at Cotopaxi characterized by a small variation in composition but spanning a wide range of intensity were studied.
- ESPs, textural data and conduit modeling were combined to investigate how magma rheology and ascent dynamics influence eruptive behavior.
- Variabilities in crystal content and magma composition result in feedbacks among crystallization, melt viscosity and volatile exsolution.

Abstract

The variability in intensity and style shown by explosive volcanism has been traditionally explained by a complex interplay among melt composition and pre-eruptive volatile content, which modulate magma ascent and conduit dynamics. However, magmas having similar compositions may be characterized by subtle textural changes affecting magma rheology and eventually explosive dynamics. Here we study five eruptions occurred at Cotopaxi volcano (Ecuador) in the last 2000 years characterized by a small variation in magma composition but spanning a wide range of intensity to investigate how these parameters control variations in eruptive intensity. We combined eruption source parameters (ESPs), obtained from the application of recent models to all the available field data, with new textural data and state-of-the-art conduit dynamics modeling. We found that, despite having variable microlite content and texture, the effect of microlite on magma rheology is partly counterbalanced by variable phenocryst abundance, resulting in a comparable total crystal content. The combination of modeling results with textural data and ESPs suggests that subtle variability in crystal content and magma composition may be accompanied by strong feedback effects among crystallization, changes in melt/magma viscosity and volatile exsolution, with microlite crystallization resulting in a rapid change of magma rheology and modifications in the explosive dynamics. By combining ESPs with quantitative textural data (i.e. melt normalized vesicle number density) and conduit modelling, we also show how general observed correlations between composition and texture of juvenile products with eruption intensity are not evident when applied to eruptions characterized by a small compositional range.

1. Introduction

Explosive eruptions are among the most spectacular and destructive phenomena on Earth. During magma rise to the surface, variable interconnected processes of degassing, bubble nucleation and growth, as well as degassing-induced crystallization, force the magma to rapidly change its rheology and eventually fragment. Once fragmentation occurs, the mixture of gas and pyroclasts is ejected at high velocity in the atmosphere forming convective volcanic plumes and/or feeding lateral pyroclastic density currents (PDCs). Recent examples of volcanic eruptions of different magnitude, such as those of Tungurahua (Ecuador, 1999), Chaitén (Chile, 2008), Eyjafjallajökull (Iceland, 2010), Cordón Caulle (Chile, 2011), Kelud and Sinabung (Indonesia, 2013-14), and Fuego (Guatemala, 2018), clearly demonstrate the variable aspects of explosive volcanism, often resulting in devastating consequences for ecosystems and population living nearby active volcanoes (e.g. Craig et al., 2016; Elissondo et al., 2016; Few et al., 2017; Martin et al., 2009; Mazzocchi et al., 2010; McCausland et al., 2019).

The large variability in intensity and style of explosive eruptions is primarily controlled by magma ascent dynamics, which modulate the Eruption Source Parameters (ESPs; e.g., exit velocity, mass eruption rate, column height), and is in turn influenced by the melt composition and pre-eruptive volatile content (Jaupart, 1996; Huppert, 2000; Gonnermann and Manga, 2007; Cashman, 2004). Basaltic explosive activity typically takes the form of low-intensity Hawaiian and Strombolian eruptions (Houghton and Gonnermann, 2008), but also sporadic, transient, higher intensity phases have been observed or described (e.g. Williams, 1983; Walker et al., 1984; McPhie et al., 1990; Rosi et al., 2006; Höskuldsson et al., 2007; Scollo et al., 2007; Coltelli et al., 1998; Costantini et al., 2009; Perez et al., 2009). Increasing magma evolution coupled with higher volatile contents is commonly associated with higher intensity activity which takes the form of sub-Plinian to Plinian eruptions, depending on their steadiness (Cioni et al., 2015). Particularly, Plinian and sub-Plinian eruptions from andesitic eruptive centers consist of multiphase eruptive episodes with shifting styles, producing complex pyroclastic successions, which have been described, among others, at Colima and Nevado de Toluca (Mexico), Somma-Vesuvius (Italy), and Taranaki and Ruapehu (New Zealand) volcanoes (e.g. Arce et al., 2003, 2005; Cioni et al., 2008; Saucedo et al., 2010; Pardo et al., 2012; Macías et al., 2017; Torres-Orozco et al., 2018).

Important progress has been made in understanding magma ascent and eruption dynamics during the last decades (Sparks, 1986; Vergniolle and Jaupart, 1986; Carey and Sigurdsson, 1989; Klug and Cashman, 1996; Melnik et al., 2005; Gonnermann and Manga, 2007), but several key questions still arise from the observation of the large variability in the eruptive style and explosive dynamics of magmas with comparable characteristics (i.e. bulk chemistry and volatile and crystal content). Such variability in eruptive style, which can even take the form of effusive-explosive transitions also in the absence of important changes in magma composition, has been related to many complex sub-surface processes such as increase in magma vesicularity, decompression-induced crystallization (predominantly microlites) and related viscosity increase, progressive loss of the exsolved fluid phase, magma shearing in the conduit, sintering, and viscous dissipation at conduit walls (Stevenson et al., 1996; Manga et al., 1998; Hammer et al., 2000; Rust et al., 2003; Polacci et al., 2001; Schipper et al., 2013; Tuffen et al., 2013; Cassidy et al., 2018; Wadsworth et al., 2020). How these processes interact with each other and to what extent they affect eruptive dynamics is however still an open question, particularly crucial for magmas having compositions spanning from basalts to andesites, for which subtle textural or compositional changes of the melt phase, often occurring syn-eruptively, may have primary effects on rheology and explosive dynamics (Mader et al., 2013; Lindoo et al., 2017; Arzilli et al. 2019a).

The last 2000 years of explosive activity of Cotopaxi, an andesitic central volcano situated in the Eastern Cordillera of the Ecuadorian Andes, offer the unique opportunity to investigate pyroclastic products of moderate- to high-intensity eruptions resulting from the ascent of andesitic magma with a restricted silica range (Barberi et al., 1995; Costantini, 2010; Pistolesi et al., 2011). Despite the similar composition (from andesite to dacite; 56 to 62 wt. % SiO_2), well-documented eruptions of this volcano present a large variability in ESPs, spanning more than one order of magnitude in mass eruption rate (MER). In this study, we selected five eruptions to discuss the factors controlling eruption dynamics in magmas of intermediate composition. ESPs of the considered Cotopaxi eruptions have been updated as part of this investigation based on the most recent available models, in order to have a comprehensive and homogenous characterization of the eruption dynamics associated with the different selected events. We thus investigated how composition, microtextural characteristics, volatile disequilibrium during magma ascent, degassing efficiency, and conduit dynamics may affect such explosive behavior.

2. Geological background and targeted eruptions

The volcanic activity in Ecuador is distributed both trench-ward and behind the volcanic arc and is related to the subduction of the oceanic Nazca plate carrying the aseismic Carnegie Ridge, produced by the passage of the plate over the Galapagos hotspot. The surface volcanism results in a broad (up to 110 km) volcanic arc (Bourdon et al., 2003) and consists of three different volcanic chains (i.e., the Western and the Eastern Cordilleras, and the Andean foothill).

Cotopaxi volcano, an ice-capped, 5897 m-high perfectly symmetrical cone, lies within the Inter-Andean valley, a structural depression within the two cordilleras. Alexander von Humboldt, explorer, geographer and naturalist, was the first European who tried to reach Cotopaxi's summit during the five years spent in South America, from 1799 to 1804. He reached an altitude of 4500 m, and only in 1872 the crater top was reached by the German geologist Wilhelm Reiss.

The volcano started its formation ~560 ka ago with the construction of an ancient stratovolcano (Paleocotopaxi), whose activity was characterized by large explosive events and deposition of rhyolitic tephra deposits (e.g., Barberi et al., 1995). After a period of potential rest, the volcanic activity resumed 100–150 ky ago (Barberi et al., 1995; Hall, 1977; Hall and Mothes, 2008) and was interrupted by a large flank failure ~4500 yr BP (Barberi et al., 1995; Hall, 1977; Hall and Mothes, 2008; Smyth and Clapperton, 1986). The scar is presently completely filled by younger products and a hummocky topography is the only remaining indication of this giant debris avalanche.

While historical chronicles concerning Cotopaxi activity are available starting from the time of the Spanish conquest, geological descriptions of Cotopaxi activity date back to the eighteenth century in a series of scientific monographs and works by La Condamine (1751), von Humboldt (1837–1838), Reiss (1874), Sodiro (1877), Stübel (1897), Whymper (1892), Wolf (1878, 1904), Reiss and Stübel (1869–1902), Hradecka et al. (1974), Miller et al. (1978), Hall (1987), Hall and von Hillebrandt (1988), and Mothes (1992). More recently, Barberi et al. (1995), Hall and Mothes (2008) and Pistolesi et al. (2011) investigated and simplified the scheme of the last andesitic eruptive cycle after the ~4500 yr BP flank failure, during which multiple scoria and pumice falls, lava and pyroclastic flows contributed to the formation of the present edifice (Table S1).

Pistolesi et al. (2011) conducted a detailed stratigraphic study related to eruptive products post-XII century which, combining field data with historical chronicles and radiocarbon ages, and highlighting the presence of 21 continuous tephra units. All these units, organized in plane-parallel sequences and separated by erosive surfaces, were characterized both physically and compositionally. The chronostratigraphic scheme covers a time window bracketed between the emplacement of the Quilotoa co-ignimbrite ash, a regional marker dated at AD 1150 (Di Muro et al., 2008; Mothes and Hall, 2008), and the last important Cotopaxi explosive event occurred in 1877, before the recent reactivation of 2015 (Gaunt et al., 2016). Barberi et al. (1995) studied the main eruptions related to a longer period of activity, starting from the sector collapse episode at ~4500 yr BP, and identified the deposits of at least 15 older eruptions (from Plinian to sub-Plinian) below the tephra Layers detailed in Pistolesi et al. (2011), including therefore eruptions over a period of time between about 2000 and 800 years ago. Hall and Mothes (2008) furtherly detailed the stratigraphic framework proposed by Barberi et al. (1995), also recognizing local deposits of lava flows and other minor pyroclastic deposits between the main eruptions.

Based on the chrono-stratigraphy and composition of the products of the recent period, Pistolesi et al. (2011) suggested that during the past eight centuries the volcanic activity was not regularly spaced over time. Between the thirteenth and eighteenth centuries, the activity was in fact characterized by isolated Plinian and sub-Plinian episodes followed by long phases of substantial degassing and suggestive of a period of low magma input rate. In the eighteenth century, the system was fueled by a significant input of volatile-rich, mafic magma, resulting in high intensity Plinian eruptions (1742-44 and 1766-68) followed by several short-lived events defining clusters of eruptions, and in a significant increase in the average eruptive rate. By revising the first-order approximation proposed by Barberi et al. (1995), who obtained an average recurrence time of 117 years dividing the time lapse of 2000 yr by the number of tephra beds counted in the same interval, Pistolesi et al. (2011) proposed that Cotopaxi was characterized by an uneven magma input rate also in the last 2000 years of activity, with periods of very frequent, low- to high-intensity activity, and scattered, mid- to high-intensity eruptions separated by longer repose intervals.

The five targeted eruptions of this study cover the last ~1000 years of activity and include Plinian and sub-Plinian events including a limited range of magma compositions. Starting from the oldest studied event, we selected the eruptions of Layers 5, 3, 2 and 1 (according to the nomenclature in Barberi et al., 1995) and the last event occurred in 1877 (layer P_E of Pistolesi et al., 2011).

Layer 5 is a fallout deposit of black scoriaceous lapilli bearing abundant lithic fragments of gray lava. Slightly younger than 1180 yr BP, Layer 5 is related to a Plinian event of andesitic composition (57.9 wt. % SiO_2). Layer 3 represents the largest Plinian pumice fallout deposit of the last 2000 years of Cotopaxi activity (Barberi et al., 1995). Dated at 820±80 yr BP, in agreement with the presence of the Quilotoa ash immediately above, the deposit is represented by a well-sorted, symmetrically-graded bed of pumice. In the upper part, a characteristic 10 cm-thick bed richer in dark lithics and lava chips is ubiquitous. Slightly more evolved than Layer 5 (62.3 wt. % SiO_2), Layer 3 is the result of a Plinian eruption. Layers 1 and 2 (M_B and M_T in Hall and Mothes, 2008 and Pistolesi et al., 2011) form a pair of black and white tephra layers traceable around the volcano resulting from Plinian activity. Interlayered stream sediments and debris-flow deposits at valley sites were scatteredly observed between these layers, as well as sporadic small pockets of organic material at the base of Layer 1. These are suggestive that the two beds were probably emplaced in a close time interval, even though they have a slightly different dispersal. Multiple tongues of loose, coarse-grained tephra deposits mainly composed of dark, cauliflower scoria bombs, which are several meters wide and up to 3 m thick and locally welded, are often found around the cone, and have been interpreted as scoria flows derived from boiling over activity during this Plinian eruption (Layer 1). Layers 2 and 1 were related to the events occurred in AD

1742–1744 and AD 1766–1768, respectively, and were associated with catastrophic lahars resulting from the rapid melting of the summit glacier. Both are andesitic in composition, with Layer 2 slightly more evolved. The last high-intensity, sub-Plinian eruption at Cotopaxi occurred in 1877 (Layer P_E in Pistolesi et al., 2011), fed by andesitic magma as well (58.8 wt. % SiO_2). Stratigraphic position and dispersal are well in agreement with detailed historical descriptions given by Wolf (1878) and Sodiro (1877) for this eruption. Scoria flows generation that accompanied the eruption was responsible for ice melting and consequent generation of destructive lahars, also well reported in the contemporary chronicles.

3. Methods

In order to study the five selected Cotopaxi eruptions, we adopted a strategy based on the integration of newly estimated ESPs (e.g., total erupted volume, column height, MER), geochemical and textural information, and conduit modeling. All the products selected for the textural studies and the physical volcanology data were collected during several field surveys carried out between 2005 and 2008. ESPs were re-calculated based on new available models for data treatment which were not available at the time of previous elaborations (e.g. Barberi et al., 1995; Pistolesi et al., 2011). New textural data of the erupted products (density, bubble size distribution and crystal content) are also included, while geochemical information is derived from the literature. All these data sources were used to constrain the input parameters of conduit simulations in order to investigate how differences in rheology, gas exsolution and crystallization may affect fragmentation and eruption dynamics. In this section, we summarize the different strategies and assumptions used to calculate the ESPs, measure textural data, and develop numerical simulations of conduit dynamics.

3.1 Eruption Source Parameters

In order to provide a comprehensive and homogeneous characterization of the five selected Cotopaxi eruptions the most recent models for the determination of ESPs have been applied and their results compared (Table 1).

First, the models of Pyle (1989), Fierstein and Nathenson (1992), and Bonadonna and Houghton (2005) had already been applied by Pistolesi et al. (2011) and Biass and Bonadonna (2011) for the determination of the tephra deposit volume. These models are based, respectively, on the integration of the Exponential applied to 1 segment (for Eruption 1877, Layers 1, 2 and 3), Exponential applied to 2 segments (for Layer 5), and Power-Law best fit of tephra-deposit thickness versus distance from the vent expressed as the square root of the area enclosed by the associated isopach contours (Fig. 1). The Power-Law limits of integration were set at 100 km (Eruption 1877, Layer 1 and Layer 2; Pistolesi et al., 2011), 100-500 km (Layer 3; Biass and Bonadonna, 2011), and 150 km (Layer 5; Biass et al., 2019). Here we have also applied the more recent model of Bonadonna and Costa (2012) that integrates the tephra-deposit volume based on the Weibull best fit (Table 1).

Second, the methods of Carey and Sparks (1986) and Rossi et al. (2019) have been used for the determination of plume height from the distribution of the largest lithics around the volcano (Fig. 1). In particular, the model of Rossi et al. (2019) builds on the model of Carey and Sparks (1986), commonly used for the determination of plume height, by implementing additional key aspects of plume dynamics, cloud spreading and particle sedimentation, such as the effect of wind advection on the buoyant plume. In fact, plumes that are bent by the action of wind have the potential to sediment a given clast size further from the vent than vertical plumes characterized by the same height. Depending on wind and eruptive conditions, the model of Rossi et al. (2019) might, therefore, return lower values of plume height with respect to the model of Carey and Sparks (1986) that only considers wind advection of particles settling in the atmosphere. The results of the models of Carey and Sparks (1986) and Rossi et al. (2019) were averaged over all lithic contours associated with the average of the 3 axis of the 5 largest clasts (i.e. 3.2 cm and 1.6 cm for Eruption 1877; 6.4 cm, 3.2 cm and 1.6 cm for Layer 1; 3.2 cm, 1.6 cm and 0.8 cm for Layer 2; 3.2 cm, 1.6 cm and 0.8 cm for Layer 3; 6.4 cm, 3.2 cm, 1.6 cm and 0.8 cm for Layer 5; Biass and Bonadonna, 2011). The determination of the plume height with the model of Carey and Sparks (1986) was carried out using the Matlab script of Biass et al. (2015) based on the crosswind and downwind ranges taken from the isopleth maps of Pistolesi et al. (2011) (Eruption 1877 and Layers 1 and 2) and of Biass and Bonadonna (2011) (Layers 3 and 5).

Finally, the strategies of Wilson and Walker (1987), Mastin et al. (2009) and Degruyter and Bonadonna (2012) have been used to determine the MER. In particular, the model of Degruyter and Bonadonna (2012) also accounts for wind advection of the buoyant plume, typically resulting in higher values of MER with respect to the models of Wilson and Walker (1987) and Mastin et al. (2009) in case of strong wind speeds. The equation of Wilson and Walker (1987) for the determination of MER was applied considering an empirical normalization constant of 0.295 as suggested by Pistolesi et al. (2011) and Biass and Bonadonna (2011) for silica-poor magmas. The application of the theoretical equation of Degruyter and Bonadonna (2012) requires values of magmatic temperature taken as 1223 K for Layer 3 (andesite) and 1273 K for Eruption 1877 and Layers 1, 2 and 5 (basaltic andesite). Additionally, the tropopause height was fixed at 17 km above sea level and wind is averaged across plume height considering the maximum value as derived using the model of Rossi et al. (2019) and a linear decay profile to sea level as suggested by Carey and Sparks (1986). It is also important to note that the vent height is taken at 5.9 km, which is especially relevant to convert to height above the vent the results derived from both the models of Carey and Sparks (1986) and Rossi et al. (2019), which are in turn expressed in height above the sampling level, averaged to be about 3 km above sea level. Such a high vent is also associated with a low atmospheric density and temperature (0.7028 kg/m^3 and 249.7 K, respectively), which largely impact the calculation of MER with the equation of Degruyter and Bonadonna (2012).

Finally, the minimum duration of the eruptions was calculated based on the combination between the peak value of MER and the Erupted Mass obtained from the average volumes of the deposits, computed considering a deposit density of 700 kg/m^3 for Eruption 1877 and Layers 2 and 3, and 950 kg/m^3 for Layers 1 and 5 (Biass and Bonadonna, 2011).

3.2 Textural data

Density of 100 randomly picked clasts (pumices or scoriae) larger than 16 mm for each layer was measured in air and water after sealing using the method of Houghton and Wilson (1989). Density data were then converted into vesicularity values using the bulk density of the samples, measured on the sample powders with a helium pycnometer. Data were then plotted as histograms and used for selecting representative clasts for vesicles and crystal image analysis.

Vesicles in pyroclastic products are the result of the complex overlapping of degassing, nucleation, expansion and eventually coalescence processes in magmas (Sparks, 1978; Cashman et al., 1994) and for this reason parameters such as size, spatial arrangements, shape as well as vesicle size distribution (VSD) and number density can be used to make inferences on the physical processes that influence the magma ascent dynamics along the volcanic conduit (Toramaru, 2006; Cashman et al., 1994; Shea et al., 2010).

VSD and vesicle number density data were estimated using 1x photo scans and Scanning Electron Microscope Back-Scattered Electrons (SEM-BSE) images of polished sections of 1 to 3 clasts of pumice and scoria from the fallout deposits of the five targeted eruptions, representative of the average, lowest and highest densities measured in these pyroclastic products. SEM-BSE images were collected at different magnifications (25×, 100×, 250× and 500×) using electron microscopy facilities in labs of the University of Geneva and MEMA center (University of Florence). Images were then analyzed using the software ImageJ (Schneider et al., 2012) to obtain the complete size distribution of the entire vesicle population. The different minerals (both phenocrysts and microlites) and vesicles recognized on the images were segmented and saved on different binary images, and their shape, size and area measured. Vesicles showing clear signs of coalescence were manually de-coalesced using the vestiges of thin septa still present along the vesicle margins, in order to obtain the original dimensional parameters of each vesicle. Data obtained from images with different magnifications were renormalized to the total area investigated in the 1× scans. 2D data from image analysis were finally reconverted to 3D using the stereological model proposed by Sahagian and Proussevitch (1998), which allows to derive N_V (number of vesicles per unit volume) from N_A (number of vesicles per unit area) and VSD in the assumption of spherical vesicles. In particular, the VSD data were obtained using a reference area (in mm^2), calculated excluding the area of vesicles touching the edge of the image as well as the area occupied by phenocrysts. Conversely, the total investigated area was used to estimate the total vesicularity and vesicle number density.

The final vesicle volume fraction for each size class V_{fi} was calculated using the values of N_V for each size class (N_{Vi}) and of the equivalent volume of each size class V_i:

$$V_{fi} = N_{Vi} \cdot V_i \quad (1)$$

Given the assumption of spherical vesicle shape, the derived values for vesicle volume fractions (V_{fi}) are generally less reliable than those obtained directly from density measurements. For this reason, V_{fi} was normalized to the total clast vesicularity as derived from the density measurements, so obtaining the adjusted volume fractions V_{fc} for each sample. By analogy, also the N_V values were normalized (N_V^m) to the melt volume (1 - φ), where φ represents the vesicle fraction derived from the density measurements (Proussevitch et al., 2007).

Phenocryst and microlite (plagioclase, clinopyroxene, ortopyroxene, oxide) contents were also measured by image analysis on selected SEM backscattered electron images. The measured data were referred to the image area excluding bubbles. Given that thin sections may be only partially representative of the largest crystals of the mineral assemblage, total crystal content was also estimated solving linear least-squares mass-balance equations with a dedicated spreadsheet, using whole-rock, residual groundmass glass and mineral phases compositions from the variable literature (Barberi et al., 1995; Pistolesi et al., 2011; Saalfeld et al., 2019; Table 2).

3.3 Conduit dynamics

The five selected eruptions, considering their similar compositions but different MERs and crystal contents, represent useful case studies to address the conditions that control the intensity of andesitic (s. l.) explosive eruptions. Thus, we investigated the conduit dynamics of the five targeted Cotopaxi eruptions (i.e., Layers 5, 3, 2, 1 and Eruption 1877) by adopting the 1D steady-state conduit model MAMMA (de’ Michieli Vitturi and Aravena, 2021). The full system of equations can be found in de' Michieli Vitturi and Aravena (2021). This two-phase numerical model accounts for the most important processes that magmas experience during ascent in the conduit, such as changes in rheology, gas exsolution, crystallization, outgassing, and magma fragmentation. The model includes a series of relaxation parameters for controlling the rate of crystallization ($\tau^{(c)}$), gas exsolution ($\tau^{(d)}$), and the pressure difference between the two phases ($\tau^{(p)}$). Here we assumed pressure equilibrium between the phases (i.e., $\tau^{(p)} \ll 1$ s), while both equilibrium and disequilibrium conditions were tested for gas exsolution (in particular, from $\tau^{(d)} = 10^{-4}\ s$ for equilibrium conditions to $\tau^{(d)} = 10\ s$ for disequilibrium conditions). Please note that larger values of $\tau^{(d)}$ tend to reproduce effusive eruptions and in other cases they delay strongly the crystallization process, which is not in agreement with textural data of some of the targeted events. Crystallization relaxation time was assumed to be large ($\tau^{(c)} = 1000$ s) in eruptions characterized by small volume fractions (< 5 vol. %) of microlites (i.e. Layer 2, Layer 3 and Eruption 1877), and of the order of $10\ s$ for eruptions that present a significant volume fraction (~30 vol. %) of microlites (i.e. Layer 1 and Layer 5; Table 2). These settings allowed us to reproduce in the numerical simulations such high contents of microlites. The reasons that can result in a delayed crystallization process (or not) are discussed below. On the other hand, modelling magma fragmentation is challenging because it can be generated by different processes in nature (e.g., Dingwell, 1996; Papale, 1999; Spieler et al., 2004; Mueller et al., 2008; Gonnermann and Manga, 2013; Cashman and Scheu, 2015; Arzilli et al., 2019b; Taddeucci et al., 2021). Brittle fragmentation in silicic magmas is expected to be triggered by high strain rates derived from the acceleration of the ascending magma or by bubble overpressure due to gas exsolution in presence of restricted bubble expansion. Instead, in low-viscosity magmas, brittle fragmentation is expected to be strongly influenced by syn-eruptive crystallization processes

(Moitra et al., 2018; Arzilli et al., 2019b). Different criteria have been implemented to describe the fragmentation position in conduit models (Gonnermann and Manga, 2013; Cashman and Scheu, 2015), including the use of a critical volume fraction of bubbles (e.g. Sparks, 1978), stress-based (e.g., Papale, 1999) and strain-based criteria (e.g., Zhang, 1999). In particular, in this work magma fragmentation is assumed to occur when a critical volume fraction of bubbles is reached, which is considered to be equal to the vesicularity measured in the volcanic products. In this way, simulations are not associated with a specific fragmentation mechanism and are simply constrained considering textural data (Table 2). In any case, note that Degruyter et al. (2012) showed that a critical gas volume fraction has similar consequences as a critical strain rate or overpressure in a one-dimensional conduit model.

As a first approximation, we also assumed isothermal conditions and cylindrical conduits, even though MAMMA allows to model depth-dependent conduit geometries (e.g. Aravena et al., 2018a; 2018b) and non-isothermal conditions (e.g. La Spina et al., 2015). Based on literature-derived information and new data of ESPs and textural information (see Section 4), we selected a set of constitutive equations to define and parametrize magma rheology, crystallization, outgassing, water exsolution and the equations of state for each studied eruption (Tables 3, S2 and captions therein). Because some eruption conditions are poorly constrained (e.g., water content, initial temperature), we considered ranges of values (Table 3; Martel et al., 2018). Inlet pressure was assumed to be equal to the lithostatic pressure, considering a conduit length of 8 km and a lithostatic pressure gradient of 25.5 MPa/km (i.e. ρ of 2600 kg/m^3). Because MER is an independently estimated parameter (basing on field data) for each one of the studied eruptions (see Table 1), for each set of input conditions, we iterated on conduit radius up to reach the conduit geometry conditions consistent with the MER values (Table 1). In this way, MER represents an input parameter of our numerical simulations, while conduit radius represents an output variable.

The outputs of MAMMA are the profiles along the conduit of key parameters such as velocity, pressure, density, crystals content and volume fraction of gas. By performing large sets of numerical simulations, we study the dependence of some model outputs on the described, uncertain input parameters (i.e. water content, temperature and equilibrium degree of gas exsolution). The measured contents of phenocrysts and microlites of each targeted eruption were adopted to recognize the input conditions (i.e. temperature, water content, equilibrium degree) that allow simulating their characteristics. When possible, we use this information to constrain key parameters of each targeted eruption, such as fragmentation depth and conduit dimensions, among others. Note that, because of computational limitations, a set of uncertain input parameters were considered fixed in our numerical simulations for a given eruption (e.g., critical volume fraction of bubbles, conduit length, inlet pressure). In fact, the results presented in this paper are based on ~15,000 conduit simulations (as a consequence of the variable input parameters and the iterative procedure to calculate the conduit radius) and thus the inclusion of additional variable inputs would have produced computational capacity problems. In any case, varying these parameters tends to show a much smaller effect on numerical results than modeled variations in water content, temperature and relaxation parameters of crystallization and gas exsolution. An additional significant simplification of our model is related to the effect of crystals in magma viscosity (Costa et al., 2007). Despite the well-documented influence of crystal size distribution and crystal shape in magma rheology (Cimarelli et al., 2011; Del Gaudio, 2014; Moitra and Gonnermann, 2015), the lack of generalized formulations able to consider the main characteristics of a system composed of phenocrysts and, eventually microlites with different shapes, hinders the consideration of more complex assumptions.

We remark that, despite the well-known limitations of numerical modeling for constraining numerically eruption conditions in presence of a series of uncertain parameters as those cited above, these results provide useful information for comparison purposes and to discuss general issues regarding high-intensity explosive eruptions driven by mildly evolved magmas.

4. Results

4.1 Eruptive Source Parameters

The five selected Cotopaxi eruptions are associated with a wide range of ESPs (Table 1). In particular, the volume of the studied tephra deposits ranges between 2.3×10^7 m^3 (Eruption 1877) and 6.0×10^8 m^3 (Layer 3) when using the method of Pyle (1989) based on the integration of the Exponential fit (Pistolesi et al., 2011; Biass and Bonadonna, 2011; Fig. 1 and Table 1). Given the limited number of isopach curves that result in a single exponential segment in most cases, the integration of the Weibull fit provides similar results to the integration of the Exponential fit. Nonetheless, the integration of the Power Law fit (Bonadonna and Houghton, 2005) results in volumes about 3 times larger, comprised between 4.9×10^7 m^3 (Eruption 1877) and 1.5×10^9 m^3 (Layer 3) (Pistolesi et al., 2011; Biass and Bonadonna, 2011; Biass et al., 2019; Table 1). In particular, the volumes of the tephra deposits of Layers 3 and 5 were also confirmed by the inversion of field data using the TEPHRA2 model (i.e. 2.4×10^9 m^3 for Layer 3 and 5.0×10^8 m^3 for Layer 3; Biass and Bonadonna, 2011). Average values of tephra-deposit volume for each eruption (excluding the inversion results) correspond to $3.2\pm1.2\times10^7$ m^3 (Eruption 1877), $2.3\pm1.1\times10^8$ m^3 (Layer 1), $3.7\pm3.5\times10^8$ m^3 (Layer 2), $8.8\pm4.4\times10^8$ m^3 (Layer 3), and $3.0\pm0.6\times10^8$ m^3 (Layer 5).

As expected, values of maximum plume height derived from the model of Rossi et al. (2019) are between 25-48% lower than those derived from the model of Carey and Sparks (1986) with the exception of the Eruption 1877, for which the difference is only 8%. Such a large difference is related to the high wind speeds associated with the eruptions of Layers 1, 2, 3 and 5. It is worth noting that the wind value reported in Table 1 corresponds to the maximum value at the tropopause, while the associated values of wind speed averaged along the plume height are 2.1 m/s, 7.2 m/s, 6.1 m/s, 6.7 m/s and 6.3 m/s for Eruption 1877, Layer 1, Layer 2, Layer 3 and Layer 5, respectively.

Finally, the peak of MER, determined with the theoretical equation of Degruyter and Bonadonna (2012) and computed using the values of maximum plume height and wind speed derived from the model of Rossi et al. (2019), results in values between 9.1×10^6 kg/s (Eruption 1877) and 5.9×10^7 kg/s (Layer 1; Table 1). These MER values are generally higher than those derived with the models of Wilson and Walker (1987) and Mastin et al. (2009) for the same sets of plume heights (with the exception of Eruption 1877), with discrepancies between 22% and 62% and between 23% and 36%, respectively. Interestingly, the model of Rossi et al. (2019), that takes into account the effect of the wind shear on plume rise, results in Layer 1 being associated with the highest plume (20.3 km above vent; a.v.), the strongest wind at tropopause (18.7 m/s) and the highest MER with the three strategies considered in this work (2.2-5.9×10^7 kg/s). In contrast, the application of the model of Carey and Sparks (1986) results in Layer 3 being associated with the highest plume (26.8 km a.v.) and the strongest wind (18.3 m/s at tropopause), so giving the highest MER with the three strategies considered here (0.7-1.9×10^8 kg/s).

The minimum duration of each eruption was derived by dividing the Erupted Mass (estimated from the average value of volume reported above and the associated deposit density) by the peak MER (calculated with the equation of Degruyter and Bonadonna, 2012) and resulted in 0.5, 1.0, 3.8, 4.8 and 2.1 hours for Eruption 1877, Layer 1, Layer 2, Layer 3 and Layer 5, respectively.

4.2 Textural data of the juvenile fraction

The studied products are moderately porphyritic with a total maximum crystal content between 16% (Layer 3) and 40% (Layer 1; Table 2). This range of values derives from a mass balance estimate considering the major elements compositions of the whole rock, glass analyses and the mineralogical assemblage. Mineralogy of juvenile clasts is characterized by a rather uniform phenocryst assemblage that includes plagioclase (max. 15%), clinopyroxene (max. 2%), orthopyroxene (max. 3%) and Fe-Ti oxides (max. 1%) as fundamental minerals. Microlite abundance is variable. In particular, the events with the lowest SiO_2 contents are characterized by a microlite content up to about 30 vol. % (Layers 1 and 5) while the events with the highest SiO_2 contents have a glassy groundmass (Eruption 1877, Layers 2 and 3). In general, microlites have skeletal features, suggestive of a rapid growth under large undercooling (e.g. Shea and Hammer, 2013).

The average clast density distribution associated with the five analyzed layers varies between 0.62 g cm^{-3} and 1.24 g cm^{-3} (55-77% density-derived clast vesicularity; Fig. 2; Table 2), with the lowest values associated with the two most evolved eruptions (Layers 2 and 3). Overall, clast density has a large, unimodal distribution (0.4-2 g cm^{-3}), with Layer 1 and Eruption 1877 showing a narrower distribution around intermediate (~1 g cm^{-3}) values. Density distribution of Layer 5 is bimodal, showing the widest variability and the highest measured density values within the studied volcanic products (Fig. 2).

Vesicle size has a polydisperse distribution, with the smallest vesicles around 8 μm and the largest around 6 mm. The smallest bubbles have a spherical to elongate shape, and the largest deformation of this bubble population is mainly visible in samples from Layer 2 and Layer 3 (Fig.

3). Clear evidence of bubble collapse only characterizes the smallest bubbles of the pumices from Eruption 1877. In the samples of all the eruptions, the largest vesicles are always irregular, probably due to processes of bubble coalescence and/or collapse. This is particularly evident in the densest products of the studied samples (Eruption 1877 and Layer 5). Overall, the Vesicle Volume Distributions (VVDs) are polymodal, with two to three distinct modes, except for products of Eruption 1877, characterized by an asymmetric, unimodal distribution, with a sharply truncated coarse tail (Fig. 3). Contrary to the highly dispersed bubble size distributions of the products from Layers 1, 2 and 5, the products of Eruption 1877 and Layer 3 are characterized by a lower dispersion of bubble size, with a marked peak around ~0.5-0.9 and ~0.3-0.6 mm, respectively (Fig. 3). The maximum bubble size of the products of Eruption 1877 is ~1.1 mm, significantly lower than that observed in the other eruptions. On the other hand, the bubble size volume distribution in the products of Layer 3 shows a secondary mode between 2 and 6 mm (Fig. 3). The diagrams of VSD (ln population density vs. size) for all the eruptions always show curved, concave upward distributions, that in some cases (Eruption 1877 and Layers 2 and 3) can be described by the combination of three main linear segments (Fig. S1)

In general, values of melt normalized vesicle number density (N_V^m) of Layers 1, 2, and 5 are similar, ranging from 1.06×10^8 to 4.80×10^8 cm^{-3}, whereas the N_V^m of the Eruption 1877 is one order of magnitude lower (1.47×10^7 cm^{-3}). The products of Layer 3 are instead characterized by the highest values of N_V^m (1.37×10^9 cm^{-3}; Fig. 3 and Table 2).

4.3 Conduit dynamics

To describe numerical results, we will focus on three of the selected eruptions: Eruption 1877, Layer 1 and Layer 3, which include volcanic products both with glassy groundmass (Eruption

1877 and Layer 3) and with ~30 vol. % of microlites (Layer 1), and also present the minimum (Eruption 1877) and maximum (Layer 1) MER and the minimum (Layer 1) and maximum (Layer 3) silica content of the studied events (Table 1). The detailed modeling results associated with the other targeted events are included in the Supplementary Material.

4.3.1 Eruption 1877

Figure 4 presents representative examples of the results derived from specific conduit simulations, selected in order to include the cases of simulations with scarce crystallization (upper panels) and with significant microlite content (lower panels). In the upper panels, we show the profiles along the conduit of key physical parameters (mixture pressure, microlite volume fraction, viscosity, gas volume fraction, dissolved water mass fraction and mixture velocity) for two simulations performed for the Eruption 1877. In these simulations, two different values for the gas exsolution relaxation parameter were used. For each simulation, the conduit radius was calculated in order to reproduce the MER of the Eruption 1877, and, in both cases, it is around 13 m. Magma ascent occurs with sparse microlite crystallization, which results in a magma characterized by a viscosity close to that of the melt near the fragmentation level. Considering the specific input conditions for these simulations (water content of 3.1 wt. % and temperature of 950°C), numerical results suggest that gas exsolution occurs from depths of about 4.5 km and fragmentation occurs at ~2.0 km depth. However, these and other results such as viscosity and exit pressure are strongly controlled by unconstrained input parameters (i.e. water content and temperature), and thus the analysis of a larger set of simulations is needed to describe properly the eruption dynamics. Under these specific circumstances, the adoption of contrasting values of the relaxation parameter for gas exsolution does not have a strong influence on the modeled dynamics of magma ascent (Fig. 4), due to the long characteristic time of magma ascent compared to the adopted values of $\tau^{(d)}$ (note that the use of larger values of $\tau^{(d)}$ result in effusive events).

Figure 5 presents a summary of the results of a set of simulations considering fixed conditions for the relaxation parameters associated with crystallization and gas exsolution (in particular, $\tau^{(c)} = 1000\ s$ and $\tau^{(d)} = 10^{-4}\ s$). The high value adopted for $\tau^{(c)}$ is here justified by the absence of an important microlite crystallization in the melt. Each panel presents a color scale of different output parameters of our simulations (fragmentation depth, conduit radius, exit pressure, exit velocity, magma viscosity at the fragmentation level and melt viscosity at the fragmentation level) as a function of initial temperature and water content. Additionally, two superposed contour maps indicate the initial volume fraction of phenocrysts (continuous contour black lines) and volume fraction of microlites (dashed contour black lines). Phenocryst volume fraction decreases when water content and temperature increase, with values between 0 vol. % and >35 vol. % for the adopted variation range of input parameters. Measured values of magma crystallinity in terms of phenocryst and microlite content (Table 2) are then used to partially constrain the field of expected variability of initial temperature, water content, and of all the other output parameters represented in Figure 5. Because the observed content of phenocrysts is about 35 vol. %, we remark that not all the combinations of water content and input temperature are compatible with the results of textural analyses of pyroclastic products of this eruption. This consideration, adopting a tolerance range of 5 vol. %, is then used to define plausible ranges of eruption conditions. Under the simulation conditions assumed for Eruption 1877 (i.e. high value of $\tau^{(c)}$), the numerical results are associated with a very low (about 3 vol. %) microlite content, in agreement with the measured data.

We also observe that narrow conduits are sufficient to produce the MER of this eruption, with values between ~12 m and ~15 m. Magma fragmentation depth ranges from ~1.5 km to ~2.2 km (Fig. 5). On the other hand, numerical simulations allow constraining other eruption parameters such as exit pressure (~10 Atm to ~20 Atm, chocked conditions) and exit velocity (~100 m/s to ~120 m/s). Magma (i.e. melt + crystals + gas) and melt viscosity at the fragmentation level range between 6.0×10^4 Pa s and 2.2×10^5 Pa s and between 6.3×10^4 Pa s and 1.4×10^5 Pa s, respectively. It is important to note that, in addition to the influence of crystals (Costa, 2005) and bubbles (Costa el al., 2007), the resulting magma viscosity at the fragmentation level is controlled by the coupled effect of magma composition, temperature, and gas volume fraction at fragmentation (i.e. the measured vesicularity of volcanic products).

Only slight changes occur in numerical results when other conditions are considered for the relaxation parameter of gas exsolution (Fig. S2). Based on our numerical results (i.e. Figs. 5 and S2), we defined a set of likely eruption conditions for Eruption 1877 that are summarized in Table 4. Some parameters can be well constrained, such as conduit dimensions and the order of magnitude of magma viscosity at the fragmentation level, while other outputs (i.e. fragmentation depth) are characterized by a significant uncertainty.

4.3.2 Layer 1

The bottom panels of Figure 4 display the profiles along the conduit of key physical parameters associated with two specific simulations performed for Layer 1. The differences in the results of simulations performed with variable values of gas exsolution relaxation parameter are here significant; conduit radius, computed through an iterative procedure with the aim of simulating the estimated MER of Layer 1, results in values of ~15.5 m (for $\tau^{(d)} = 10^{-4}\, s$) and ~17 m (for

$\tau^{(d)} = 10\,s$). In contrast to the upper panels of Figure 4, these simulations were performed in order to accomplish a significant crystallization of microlites as observed in the natural samples of this eruption (i.e. using a lower value for $\tau^{(c)}$), which results in a larger difference between the magma viscosity and melt viscosity at the fragmentation level.

Figure 6 displays the results associated with a set of simulations performed for Layer 1, for which we considered fixed conditions for the relaxation parameters related to crystallization ($\tau^{(c)} = 10\,s$) and gas exsolution ($\tau^{(d)} = 10^{-4}\,s$). Phenocryst volume fraction ranges between 0 vol. % and >40 vol. % for the modeled range of water content and temperature. Again, we highlight that not all the combinations of water content and input temperature are compatible with the phenocrysts content measured for this eruption (about 20 vol. %). The low value adopted for $\tau^{(c)}$ allows for significant microlite crystallization, reaching concentrations of the order of 30 vol. %, in agreement with the texture observed in the associated volcanic products. In this case as well, these considerations were used to define plausible ranges of eruption conditions, which are less constrained (especially in terms of water content) respect to what observed for the Eruption 1877 simulations. It is worth highlighting that larger values of $\tau^{(c)}$ and $\tau^{(d)}$ are not able to model the observed concentration of microlites and thus their results are not included here.

The higher MER associated with Layer 1 reflects into larger conduits, with a maximum range for radius between ~14 m and ~19 m. Fragmentation depths compatible with phenocrysts and microlites contents vary between ~0.3 km and ~1.0 km, while exit pressure and exit velocity ranges between ~60 Atm and ~120 Atm and from ~130 m/s to ~190 m/s, respectively. Finally, magma and melt viscosity at the fragmentation level range between 9.1×10^{3} Pa s and 8.7×10^{4} Pa s and between 6.9×10^{3} Pa s and 1.9×10^{4} Pa s, respectively. The differences between magma and melt viscosity derive in this case from the dominant effect of crystals (Costa, 2005).

Figure S3 presents the equivalent results associated with disequilibrium conditions of gas exsolution. Based on these results (i.e., Figs. 6 and S3), a set of likely eruption conditions for Layer 1 was defined, presented in Table 4. Please note that differences between the results summarized in Table 4 and the description presented in the previous paragraph for Figure 6 are small.

4.3.3 Layer 3

Layer 3 represents an end-member for the five selected eruptions, showing the most evolved magma composition coupled with a very low crystal content. In Figure 7, we present the results of a set of simulations performed for this eruption, considering $\tau^{(c)} = 1000\ s$ and $\tau^{(d)} = 10^{-4}\ s$. The volume fraction of phenocrysts varies between 0 vol. % and ~30 vol. % for the adopted values of water content and temperature. Also in this case, only a restricted portion of the panels presented in Figure 7 is compatible with the content of phenocrysts measured in the products of Layer 3 (about 10 vol. %) allowing to define plausible ranges for eruption conditions. On the other hand, the value adopted for $\tau^{(c)}$ is manifested in sparse crystallization, compatible with the characteristics of this eruption. In this case, the very low content of microlites in all the simulations reflects in a less robust constrain for eruption conditions, at least in terms of initial water content and temperature.

The results presented in Figure 7 suggest a conduit radius between ~13 m and ~18 m for Layer 3. Fragmentation depths compatible with textural data vary between ~0.1 km and ~1.2 km, exit pressure ranges from ~40 Atm to ~90 Atm, and exit velocity varies between ~130 m/s and ~190 m/s. On the other hand, magma and melt viscosity at the level of fragmentation vary between 6.5×10^3 Pa s and 6.6×10^4 Pa s and between 5.6×10^4 Pa s and 3.8×10^5 Pa s, respectively.

The equivalent results derived from disequilibrium conditions of gas exsolution are displayed in Figure S4. From these results (i.e., Figs. 7 and S6), we defined likely eruption conditions for Layer 3 (Table 4). Numerical results associated with Layers 2 and 5 are presented in Figures S4, S5, S7, and S8 and a summary of the derived constraints for key eruption parameters is included in Table 4.

5. Discussion

5.1 Conduit modeling and eruption dynamics

Given the significant range of ESPs for the recent activity at Cotopaxi volcano, and based on the limited range of magma compositions involved in this activity, we emphasize the importance of having accurate parameters (both textural and physical) in order to address and discuss how magma rheology may affect eruption dynamics. To accomplish this, we revised all the available field data in order to retrieve ESPs based on the most recent models, which were then combined with detailed textural analyses of the juvenile products and with state-of-the-art conduit dynamics modeling.

Results summarized in Table 4 indicate only slight differences for the radius of the conduit associated with all eruptions, suggesting that other factors controlled the variability of MER of the studied eruptions (Fig. 8a). Instead, there is a good correlation among MER and dynamic features of the erupting mixture such as exit pressure and exit velocity, with the eruptions characterized by the highest values of MER (i.e. Layers 1 and 5) having also the highest contents of microlites and the highest exit pressures (50 – 120 Atm) and velocities (130 – 190 ms^{-1}). Conversely, the eruptions with products characterized by a glassy groundmass (i.e. Eruption 1877 and Layer 2) have exit pressures lower than 40 Atm coupled with a low exit velocity (90 – 130 ms^{-1}; Fig. 8b, c).

Layer 3, which is significantly richer in SiO_2 than the other targeted eruptions, presents intermediate results for the two variables. Interestingly, the event characterized by the lowest values of exit pressure and velocity (i.e. Eruption 1877) is also associated with boiling-over activity resulting in the emplacement of widespread scoria flow deposits during the eruption (Barberi et al., 1995; Pistolesi et al., 2011). The presence of a crater (well visible at Cotopaxi) could have modulated the decompression of the jet: according to the numerical results of Woods and Bower (1995), jets with a low overpressure can rapidly decompress well below the external pressure and re-equilibrate through a shock wave inside the crater. This recompression results in a drastic change of the mixture velocity and hence in a low fountaining of the column feeding the boiling over activity.

Although fragmentation depth could not be unequivocally constrained, significant differences have been recognized among the studied eruptions, showing a general decrease with increasing MER; in this context, those eruptions with a higher groundmass crystallinity (Layers 1 and 5) also show the shallowest fragmentation depth (Fig. 8d).

An unclear relationship is shown between MER and magma (i.e. melt + crystals + bubbles) viscosity at the fragmentation depth (Fig. 8e), with the events with the highest MER also having the lowest magma viscosity at this level. Similar, high values of MER characterize both eruptions with the lowest SiO_2 contents (Layers 1 and 5) and Layer 3, which shows the highest SiO_2 content. Interestingly, even though it is well known that silica content is positively correlated with melt viscosity (e.g. Giordano et al., 2008), the influence of microlites, more abundant in the eruptions characterized by the lowest contents of silica (and highest MER), results in an apparent lower value of magma viscosity at the fragmentation level (Fig. 8f). This counter-intuitive result, which is also manifested in an apparent lack of correlation between MER and silica content, highlights the critical importance of crystallization in controlling the eruption dynamics of intermediate magmas.

5.2 Texture, composition and eruptive source parameters

Size distributions of vesicles from the different eruptions show variable characteristics. Data from Layer 1 and Layer 5 suggest similar conditions of vesiculation, with a quite large size range covered by the vesicles, a negligible amount of vesicle coalescence and clearly concave upward VSD plots, suggesting continuous/accelerating bubble nucleation and growth (Shea et al., 2010; Fig. S1). This was possibly accomplished by a relatively low magma ascent velocity (averaged along the conduit), which allowed also the occurrence of an important, degassing-induced, microlite crystallization. The high exit pressure suggested for these two eruptions by the modeling results (Table 4) is in general agreement with this interpretation. Pumice clasts from Layer 2 and Layer 3 present clear multimodal VVDs (Fig. 3), suggestive of a complex vesiculation history. However, while the vesicle size distribution of Layer 3 can be interpreted as related to the presence of important coalescence effects on a distribution characterized by a curved, concave upward trend, the complex VVD diagram of Layer 2 (Fig. 3), associated with a VSD curve characterized by three different segments (Fig. S1), reveals the occurrence of few, distinct episodes of vesiculation during ascent. The ESPs and dynamical parameters estimated for Layer 3 (high MER, high exit pressure and velocity, shallow fragmentation depth) are all indicative of a large eruption characterized by a rapid, continuous and accelerating process of magma ascent, decompression and degassing, well recorded by the general features of vesicle shape and size. Pumices from the Eruption 1877 show the largest variability in terms of vesicle distribution; these are in fact characterized by important differences in shape and volume density of bubbles, and by the presence, in most of the samples, of collapsed vesicles. The shape of the VSD and CVD (Figs. 3, S1) diagrams suggest the presence of few, distinct episodes of vesicle nucleation and growth. The small conduit radius related to this eruption (Table 4), inducing important lateral gradients in the ascending magma column, could explain the large variability observed in the texture of the vesicular material. The partial outgassing of the magma (suggested by the presence of collapsed vesicles) was however not sufficient to force an important microlite crystallization (low undercooling?).

A positive correlation between N_V^m and whole-rock SiO_2 content of the studied samples exists for the products of Layers 1, 2, 3 and 5 (Fig. 9a). An important discrepancy from this linear trend occurs for the Eruption 1877 products, which show a lower value of N_V^m respect to that observed for similar compositions. However, the texture of these products reveals clear evidence of open-degassing behavior, which could have largely reduced the vesicle number density. The variation of the general texture of the analyzed products with the increase of SiO_2 content suggests that the more evolved compositions are characterized by smaller and more deformed (although still with convex shapes) bubbles, with bubble walls thinner than the other products (Fig. 3). In general, we observe a variation of the texture of Cotopaxi products with increasing SiO_2 content, even though in a limited range (Table S3). However, it is worth noting that these products are characterized by significant differences in glass matrix composition due to the differences in crystal content, with a transition from andesitic (Layers 1 and 5) to dacitic (Eruption 1877, Layer 2 and Layer 3), where the greatest changes in bubble texture seem to be recorded. Despite this rough correlation among silica content and N_V^m, no clear relationship exists among N_V^m and MER (Fig. 9b), possibly related to the fact that for 3 out of 5 eruptions the MER variability spans a range of values that lie within the associated errors. A clear negative correlation also exists between N_V^m and magma viscosity (Fig. 9e, f), suggesting that bubble nucleation (+ resorption) may be hindered at high viscosity. This is particularly evident for Eruption 1877, for which the lowest N_V^m is clearly associated with vesicle resorption and collapse. Unexpectedly, we observe a positive correlation between N_V^m and total erupted volume (Fig. 9c). The significance of this clear correlation is somewhat obscure, and it should be possibly linked with the complex interactions between the dynamics of reservoir emptying and the associated pressure changes, that could in turn reflects onto the dynamics of bubble growth. The absence of a clear correlation between parameters like MER, silica content or melt viscosity and vesicle number density suggests that the relation evidenced by Toramaru (2006) among some of these parameters should be accurately reconsidered, particularly when looking at restricted silica variability.

5.3 Controls of magma features on eruptive parameters in eruptions of intermediate magma compositions

In order to explain how eruption dynamics (e.g. MER) may be controlled by pre-eruptive parameters and magma rheology, we have combined here textural data, ESPs and dynamic parameters derived from numerical modeling. Unfortunately, we have no direct data for pre-eruptive volatile (water) content of the magma, although a rough indirect estimation can be derived from fitting the results of numerical modeling (Figs. 5, 6, 7 and S2 to S8) with some observables. The aim of this discussion is to show any possible relation between the observed or inferred magma features (composition, crystal content, N_V, water content, viscosity) and measured or modeled dynamical parameters. Eruptions characterized by the most mafic compositions also correspond to the most crystallized samples (Layers 1 and 5); modeling results suggest that these eruptions were possibly associated with volatile-rich magmas (H_2O > 3.5 wt. %) and a relatively low melt viscosity (Figs. 6, S3, S7, S8). All these conditions possibly favored eruptive dynamics dominated by the highest MER and the highest exit pressures and velocities.

High volatile contents (Figs. 7 and S6) also characterized the SiO_2-richer magma of Layer 3, erupted at high MER but without developing a diffuse groundmass crystallization. The high melt viscosity and the rapid magma ascent could have forced in this case an important delay in syn-eruptive vesiculation, forced to occur at high overpressure over a short length below the fragmentation level and so resulting in a high N_V value and a poorly dispersed (except for the effects of coalescence) vesicle size distribution (Fig. 3).

A glassy groundmass also characterizes the products of Layer 2 and Eruption 1877, having an intermediate composition and a low volatile content. These eruptions have the lowest MER between the five targeted events, and clearly differentiate respect to the two crystal-rich eruptions discussed above. Despite their similarity in terms of some of the most important dynamical or compositional parameters, these two events clearly differ for the dynamics of magma degassing as recorded in the textural features of their products (Fig. 3).

As a whole, two end members can be observed for texture of the melt, one having a very low (0-2%) microlite content (Eruption 1877, Layers 2 and 3), and one with high (30%) microlite content (Layers 1 and 5), with no group having intermediate characteristics. The microlite texture is however partly counterbalanced by phenocryst abundance, resulting in total crystal content of 16 to 40 wt. %. Despite a range in matrix glass composition (andesitic to dacitic) due to variable microlite content, overall crystallinity is thus partly counterbalanced by phenocryst abundance, resulting in a more subtle variability among the studied eruptions. This, coupled to a small range of bulk-rock composition, may suggest strong feedbacks effects among crystallization, changes in melt/magma viscosity and volatile exsolution. Once started, the process of microlite crystallization may result in a rapid change in magma rheology, further enhancing gas exsolution and microlite formation, with the latter becoming rapidly dominant during magma ascent.

It has been suggested that magma characteristics (i.e. composition and texture) scale with eruption intensity (i.e. MER). In particular, although the relationship between the evolution of the volatile fraction within the melt and the explosivity of the eruption is not totally understood, bubble number density vs. SiO_2 (Toramaru, 2006) and MER vs. N_V^m (Alfano et al., 2012; Houghton et al., 2010) were used to suggest a positive correlation between intensity and tephra texture. On one hand, this general correlation cannot be generalized to all cases, and it is limited to those cases in which vesiculation occurs under near-equilibrium condition, as shown by Rust and Cashman (2011). In fact, while at a broader scale the trend may appear evident, different behaviors can be extrapolated when considering the diverse compositional sub-groups (e.g. basaltic, phonolitic, andesitic-rhyolitic; Alfano et al., 2011), with further complications related to microlite abundance (Moitra et al., 2013). Our data further confirm that, when considering a small range of magma composition, the observed variability in MER is coupled to a wide range of vesicle number densities which barely define a clear trend. This apparent scatter suggests that, at comparable degree of magma evolution (in our case 59.5<whole rock SiO_2 wt.%<64.9), other factors (e.g. magma ascent velocity, degree of undercooling and microlite nucleation and growth) are at play in governing conduit dynamics, with bubble nucleation and evolution resulting in complex size distributions and largely variable N_V^m values. For the studied eruptions, we envisage that the combination of variable (0-2% to 30%) microlite contents with different phenocryst abundances (total crystal content range of 16 - 40 wt.%) may eventually control eruption dynamics which, despite a limited variability of bulk magma composition, resulted in a wide range of ESPs, as retrieved from deposit studies. Also, modeling results suggest this variability, with microlite-rich mafic eruptions (L1, L5) showing high MDR, exit pressure, velocity and water content despite a low melt viscosity, and more evolved cases (L2 and 1877) having lower water content and dynamical parameters coupled to a glassy groundmass and a higher viscosity. As a matter of fact, the presented data demonstrate the existence of fully non-linear, complex inter-relationships between the different dynamical and textural parameters, warning about the use of simple (or simplistic) relations for deriving general laws. The example of Cotopaxi is particularly relevant in showing that this complexity can characterize a very limited range of magma compositions which however resulted in eruptive events having ESPs spanning two orders of magnitude. It has recently shown that for rhyolitic compositions and under homogeneous nucleation conditions, a general trend predicted by the bubble number density decompression rate meter of Toramaru (2006) still holds for $N_V>10^7$ cm^{-3} (Hajimirza et al., 2019), while the relation cannot be applied when N_V is lower for diffusion to affect saturation. Decompression-independent bubble number densities in decompression experiments, albeit in hydrated phonolitic melts, has been shown by Allabar and Nowak (2018). The little or no dependency of number density on eruption intensity (or decompression rate) that we observe here may be ascribed to the large textural variability (e.g. microlite content) and volatile saturation conditions, which may result in a complex interplay between diffusion and decompression nearly unrelated to the slight compositional variability.

6. Conclusions

Explosive behavior of volcanoes results from the complex interplay among initial magma properties and ascent dynamics along the conduit. This interplay in turn modulates continuous changes in extensive and intensive parameters before final magma fragmentation. By examining five eruptions occurred at Cotopaxi volcano, we had the opportunity of exploring how events characterized by a small variation in magma composition resulted in explosive events spanning a wide range of intensity, from sub-Plinian to Plinian. To accomplish this, we combined both textural and physical parameters in order to address and discuss how magma rheology may affect eruption dynamics. All the available field data were revised in order to retrieve ESPs based on the most recent models, which were then combined with detailed textural analyses of the juvenile products and with state-of-the-art conduit dynamics modeling. We found that the five selected eruptions can be grouped in two end members in relation to texture of the products, one having a very low (0-2%) and one high (30%) microlite content. Nonetheless, the effect of microlite content is partly counterbalanced by phenocryst abundance, resulting in total crystal content of 16 to 40 wt. %. The combination of conduit modeling results with textural data and ESPs suggests that subtle variability in crystal content and magma composition may be accompanied by strong feedbacks effects among crystallization, changes in melt/magma viscosity and volatile exsolution, with microlite crystallization resulting in a rapid change in magma rheology and eventually in different explosive dynamics.

Finally, we also emphasize that the general observed correlation among magma characteristics (i.e. composition and texture) with eruption intensity (i.e. MER) may be problematic when applied to eruptions characterized by small compositional variability. While at a broader scale the trend may be evident, particularly considering compositional sub-groups (e.g. basaltic, phonolitic, andesitic-rhyolitic), we show that, when dealing with subtle variations in magma composition, the observed variability in MER is coupled to a variety of textural characteristics (i.e. number densities) such that the definition of a clear trend results problematic. Data scattering may be related to a complex series of parameters at play (magma ascent velocity, degree of undercooling and microlite nucleation and growth) resulting in very different explosive dynamics despite the limited compositional range.

Acknowledgements

The authors would like to thank all the involved institutions for the technical support during sample preparation and analytical sessions. We are also thankful to E. Rossi and W. Degruyter for constructive discussion. M. Edmonds and one anonymous reviewer are acknowledged for useful comments. This study was supported by the Swiss National Science Foundation (project #200020_188757). AA was financed by the French government IDEX-ISITE initiative 16-IDEX-0001 (CAP 20-25). The data on which this article is based are available in Barberi et al. (1995), Costantini et al. (2005), Biass and Bonadonna (2011), Pistolesi et al. (2011), Biass et al. (2019) and Saalfeld et al. (2019). Conduit modelling was performed with the MAMMA code (de' Michieli Vitturi and Aravena, 2021) available at https://github.com/demichie/MAMMA and at https://vhub.org/resources/mamma. Plume heights were calculated with the Matlab script of Biass et al. (2015) available at https://github.com/e5k/CareySparks86_Matlab and at https://vhub.org/resources/3922.

Authors' contribution

Conceptualization: M. Pistolesi, C. Bonadonna, R. Cioni. Formal analysis: L. Costantini, C. Vigiani, A. Aravena. Investigation: M. Pistolesi, C. Bonadonna, R. Cioni. Methodology: C. Costantini, C. Bonadonna, A. Aravena. Resources: M. Pistolesi, C. Bonadonna, R. Cioni. Supervision: M. Pistolesi, R. Cioni, C. Bonadonna. Validation: M. Pistolesi, C. Bonadonna, R.

Cioni., A. Aravena. Writing-original draft: M. Pistolesi, A. Aravena. Writing-review & editing: M. Pistolesi, A. Aravena, R. Cioni, C. Bonadonna.

References

Alfano, F., Bonadonna, C., Gurioli, L. (2012). Insights on rhyolitic eruption dynamic from textural analysis: the example of the May Chaitén eruption (Chile). Bull. Volcanol. 74(9):2095–2108. https://doi.org/10.1007/s00445-012-0648-3

Allabar, A., & Nowak, M. (2018). Message in a bottle: Spontaneous phase separation of hydrous Vesuvius melt even at low decompression rates. Earth and Planetary Science Letters, 501, 192–201. https://doi.org/10.1016/j.epsl.2018.08.047

Aravena, A., Cioni, R., de' Michieli Vitturi, M., & Neri, A. (2018a). Conduit stability effects on intensity and steadiness of explosive eruptions. Scientific Reports, 8(1), 1-9. https://doi.org/10.1038/s41598-018-22539-8

Aravena, A., Cioni, R., de' Michieli Vitturi, M., Pistolesi, M., Ripepe, M., & Neri, A. (2018b). Evolution of conduit geometry and eruptive parameters during effusive events. Geophysical Research Letters, 45(15), 7471-7480. https://doi.org/10.1029/2018GL077806

Arce, J.L., Macías, J.L., & Vázquez, S.L. (2003). The 10.5 ka Plinian eruption of Nevado de Toluca, México: Stratigraphy and hazard implications. Geological Society of America Bulletin, 115, 2, 230–248.

Arce, J.L., Cervantes, K.E., Macías, J.L., & Mora, J.C. (2005). The 12.1 ka Middle Toluca Pumice: A dacitic Plinian–subplinian eruption of Nevado de Toluca in central Mexico. Journal of Volcanology and Geothermal Research, 147, 125-143.

Arzilli, F., Morgavi, D., Petrelli, M., Polacci, M., Burton, M., Di Genova, D., Spina, L., La Spina,G., Hartley, M.E., Romero, J.E., Fellowes, J., Diaz-Alvarado, J., Perugini, D. (2019a).The un-expected explosive sub-Plinian eruption of Calbuco volcano (22–23 April 2015;southern Chile): Triggering mechanism implications. Journal of Volcanology and Geothermal Research, 378, 35–50.

Arzilli, F., La Spina, G., Burton, M. R., Polacci, M., Le Gall, N., Hartley, M. E., Di Genova, D., Cai, B., Vo, N. T., Bamber, E. C., Nonni, S., Atwood, R., Llewellin, E. W., Brooker, R. A., Mader, H. M., & Lee, P. D. (2019b). Magma fragmentation in highly explosive basaltic eruptions induced by rapid crystallization. Nature Geoscience, 12(12), 1023-1028.

Barberi, F., Coltelli, M., Frullani, A., Rosi, M., & Almeida, E. (1995). Chronology and dispersal characteristics of recently (last 5000 years) erupted tephra of Cotopaxi (Ecuador): Implications for long-term eruptive forecasting: Journal of Volcanology and Geothermal Research, v. 69, p. 217–239, https://doi.org/10.1016/0377-0273(95)00017-8

Biass, S., Bagheri, G., & Bonadonna, C. (2015). A Matlab implementation of the Carey and Sparks (1986) model. https://vhub.org/resources/3922

Biass, S., & Bonadonna, C. (2011). A quantitative uncertainty assessment of eruptive parameters derived from tephra deposits: the example of two large eruptions of Cotopaxi volcano, Ecuador. Bulletin of Volcanology, 73(1), 73-90. https://doi.org/10.1007/s00445-010-0404-5

Biass, S., Bonadonna, C., & Houghton, B. F. (2019). A step-by-step evaluation of empirical methods to quantify eruption source parameters from tephra-fall deposits. Journal of Applied Volcanology, 8(1), 1-16. https://doi.org/10.1186/s13617-018-0081-1

Bonadonna, C., & Costa, A. (2012). Estimating the volume of tephra deposits: a new simple strategy. Geology, 40(5), 415-418.

Bonadonna, C., & Houghton, B. F. (2005). Total grain-size distribution and volume of tephra-fall deposits. Bulletin of Volcanology, 67(5), 441-456.

Bourdon, E., Eissen, J.-P., Gutscher, M.-A., Monzier, M., Hall, M.L., & Cotton, J. (2003). Magmatic response to early aseismic ridge subduction: The Ecuadorian margin case (South America): Earth and Planetary Science Letters, v. 205, p. 123–138, doi: 10.1016/S0012-821X(02)01024-5.

Botcharnikov, R. E., Holtz, F., & Behrens, H. (2015). Solubility and fluid–melt partitioning of H2O and Cl in andesitic magmas as a function of pressure between 50 and 500 MPa. Chemical Geology, 418, 117-131.

Carey, S., & Sigurdsson, H. (1989). The intensity of plinian eruptions. Bulletin of Volcanology, 51(1), 28-40.

Carey, S., & Sparks, R. S. J. (1986). Quantitative models of the fallout and dispersal of tephra from volcanic eruption columns. Bulletin of Volcanology, 48(2), 109-125.

Cashman, K.V. (2004). Volatile controls on magma ascent and eruption, in Sparks, R.S.J., and Hawkesworth, C.J., The State of the Planet: Frontiers and Challenges in Geophysics: Geophysical Monograph 150: Washing-ton, D.C., American Geophysical Union, p. 109–124, doi:10.1029/150GM10.

Cashman, K. V., Mangan, M. T., & Newman, S. (1994). Surface degassing and modifications to vesicle size distributions in active basalt flows. Journal of Volcanology and Geothermal research, 61(1-2), 45-68.

Cashman, K. V., & Scheu, B. (2015). Magmatic fragmentation. In: The encyclopedia of volcanoes (pp. 459-471). Academic Press.

Cassidy, M., Manga, M., Cashman, K., & Bachmann, O. (2018). Controls on explosive-effusive volcanic eruption styles. Nature Communications, 9(1), 1-16.

Cimarelli, C., Costa, A., Mueller, S., & Mader, H. M. (2011). Rheology of magmas with bimodal crystal size and shape distributions: Insights from analog experiments. Geochemistry, Geophysics, Geosystems, 12(7).

Cioni, R., Bertagnini, A., Santacroce, R., & Andronico, D. (2008). Explosive activity and eruption scenarios at Somma-Vesuvius (Italy): Towards a new classification scheme. Journal of Volcanology and Geothermal Research, 178, 331–346.

Cioni, R., Pistolesi, M., & Rosi, M. (2015). Plinian and subplinian eruptions. In The Encyclopedia of Volcanoes (pp. 519-535). Academic Press.

Coltelli, M., Del Carlo, P., & Vezzoli, L. (1998). Discovery of a Plinian basaltic eruption of Roman age at Etna volcano, Italy. Geology, 26(12), 1095-1098.

Costa, A. (2005). Viscosity of high crystal content melts: dependence on solid fraction. Geophysical Research Letters 32.

Costa, A., Melnik, O., Sparks, R. & Voight, B. (2007). Control of magma flow in dykes on cyclic lava dome extrusion. Geophysical Research Letters 34.

Costantini, L. (2010). Understanding basaltic explosive volcanism (Doctoral dissertation, University of Geneva).

Costantini, L., Bonadonna, C., Houghton, B. F., & Wehrmann, H. (2009). New physical characterization of the Fontana Lapilli basaltic Plinian eruption, Nicaragua. Bulletin of Volcanology, 71(3), 337.

Craig, H., Wilson, T., Stewart, C., Villarosa, G., Outes, V., Cronin, S., & Jenkins, S. (2016). Agricultural impact assessment and management after three widespread tephra falls in Patagonia. South America. Natural Hazards, 82(2), 1167-1229.

de' Michieli Vitturi, M., & Aravena, A. (2021). Numerical modeling of magma ascent dynamics. In: Forecasting and Planning for Volcanic Hazards, Risks, and Disasters, Elsevier. https://doi.org/10.1016/B978-0-12-818082-2.00006-8

Degruyter, W., Bachmann, O., Burgisser, A., & Manga, M. (2012). The effects of outgassing on the transition between effusive and explosive silicic eruptions. Earth and Planetary Science Letters, 349, 161–170. https://doi.org/10.1016/j.epsl.2012.06.056

Degruyter, W., & Bonadonna, C. (2012). Improving on mass flow rate estimates of volcanic eruptions. Geophysical Research Letters, 39(16).

Del Gaudio, P. (2014). Rheology of bimodal crystals suspensions: Results from analogue experiments and implications for magma ascent. Geochemistry, Geophysics, Geosystems, 15(1), 284-291.

Di Muro, A., Rosi, M., Aguilera, A., Barbieri, R., Massa, G., Mundula, F., and Pieri, F. (2008). Transport and sedimentation dynamics of transitional explosive eruption columns: The example of the 800 BP Quilotoa Plinian eruption (Ecuador): Journal of Volcanology and Geothermal Research, v. 174, p. 307–324, doi: 10.1016/j .jvolgeores.2008.03.002.

Dingwell, D. B. (1996). Volcanic dilemma--flow or blow? Science, 273(5278), 1054-1055.

Elissondo, M., Baumann, V., Bonadonna, C., Pistolesi, M., Cioni, R., Bertagnini, A., Biass, S., Herrera, J.C., and Gonzalez, R. (2016). Chronology and impact of the 2011 Cordón Caulle eruption, Chile. Natural Hazards and Earth System Sciences, 16(3), 675-704.

Few, R., Armijos, M.T., & Barclay, J. (2017). Living with Volcan Tungurahua: the dynamics of vulnerability during prolonged volcanic activity. Geoforum, 80, 72-81.

Fierstein, J., & Nathenson, M. (1992). Another look at the calculation of fallout tephra volumes. Bulletin of Volcanology, 54(2), 156-167.

Gaunt, H. E., Bernard, B., Hidalgo, S., Proaño, A., Wright, H., Mothes, P., ... & Kueppers, U. (2016). Juvenile magma recognition and eruptive dynamics inferred from the analysis of ash time series: The 2015 reawakening of Cotopaxi volcano. Journal of Volcanology and Geothermal Research, 328, 134-146.

Giordano, D., Russell, J. K. & Dingwell, D. B. (2008). Viscosity of magmatic liquids: a model. Earth and Planetary Science Letters 271, 123-134.

Gonnermann, H. M., & Manga, M. (2007). The fluid mechanics inside a volcano. Annu. Rev. Fluid Mech., 39, 321-356.

Gonnermann, H. M., & Manga, M. (2013). Dynamics of magma ascent in the volcanic conduit. In: Modeling volcanic processes: The physics and mathematics of volcanism, pp. 55-84.

Hajimirza, S., Gonnermann, H. M., Gardner, J. E. & Giachetti, T. (2019). Predicting homogeneous bubble nucleation in rhyolite. Journal of Geophysical Research, 124, 2395–2416.

Hall, M. (1977). El Volcanismo en el Ecuador: Quito, Instituto Panamericano de Geografía e Historia, 120 p.

Hall, M. (1987). Peligros potenciales de las erupciones futu-ras del volcán Cotopaxi: Escuela Politécnica Nacional Monografía de Geología 5/12, p. 41–80.

Hall, M., & Mothes, P. (2008). The rhyolitic–andesitic erup- tive history of Cotopaxi volcano, Ecuador: Bulletin of Volcanology, v. 70, p. 675–702, doi: 10.1007/s00445 -007-0161-2.

Hall, M., & von Hillebrandt, C. (1988). Mapa de los Peligros Volcánicos Potenciales Asociados con el Volcán Coto-paxi: Zona Norte: Quito, Ecuador, Instituto Geofísico, Escuela Politécnica Nacional, scale 1:50.000.

Hammer, J. E., Cashman, K. V., & Voight, B. (2000). Magmatic processes revealed by textural and compositional trends in Merapi dome lavas. Journal of Volcanology and Geothermal Research, 100(1-4), 165-192.

Höskuldsson, Á., Óskarsson, N., Pedersen, R., Grönvold, K., Vogfjörð, K., & Ólafsdóttir, R. (2007). The millennium eruption of Hekla in February 2000. Bulletin of Volcanology, 70(2), 169-182.

Houghton, B. F., & Gonnermann, H. M. (2008). Basaltic explosive volcanism: constraints from deposits and models. Geochemistry, 68(2), 117-140.

Houghton, B. F., & Wilson, C. J. N. (1989). A vesicularity index for pyroclastic deposits. Bulletin of Volcanology, 51(6), 451-462.

Houghton, B.F., Carey, R.J., Cashman, K.V., Wilson, C.J.N., Hobden, B.J., Hammer, J.E. (2010). Diverse patterns of ascent, degassing, and eruption of rhyolite magma during the 1.8 ka Taupo eruption, New Zealand: evidence from clast vesicularity. J. Volcanol. Geoth. Res. 195(1):31–47.

Hradecka, L., Hradecky, P., Kruta, M., Lysenko, V., Mlcoch, B., & Paulo, A. (1974). La Exploración Geológica de Volcán Cotopaxi en el Ecuador: Prague, Czech Republic, Instituto Geologico Central, 61 p.

Huppert, H. E. (2000). Geological fluid mechanics. In: Batchelor GK, Moffatt HK, Worster MG (eds), Perspectives in Fluid Dynamics: A Collective Introduction to Current Research. Cambridge University Press, 447-506.

Jaupart, C. (1996). Physical models of volcanic eruptions. Chemical Geology, 128(1-4), 217-227.

Klug, C., & Cashman, K. V. (1996). Permeability development in vesiculating magmas: implications for fragmentation. Bulletin of Volcanology, 58(2-3), 87-100.

La Condamine, Ch.M. (1751). Diario del Viaje al Ecuador. Introducción Histórica a la Medición de los Tres Primeros Grados del Meridiano: Coloquio "Ecuador 1986": Quito, Ecuador, Editorial Publitécnica, translated by Eloy Soria Sánchez (1986), 222 p.

La Spina, G., Burton, M., & de' Michieli Vitturi, M. (2015). Temperature evolution during magma ascent in basaltic effusive eruptions: A numerical application to Stromboli volcano. Earth and Planetary Science Letters, 426, 89-100.

Le Métayer, O., Massoni, J., & Saurel, R. (2005). Modelling evaporation fronts with reactive Riemann solvers. Journal of Computational Physics, 205(2), 567–610.

Lindoo, A., Larsen, J.F., Cashman, K.V., Oppenheimer, J. (2017). Crystal controls on permeability development and degassing in basaltic andesite magma. Geology, 45 (9): 831–834. https://doi.org/10.1130/G39157.1

Llewellin, E. W., & Manga, M. (2005). Bubble suspension rheology and implications for conduit flow. Journal of Volcanology and Geothermal Research, 143(1-3), 205-217. https://doi.org/10.1016/j.jvolgeores.2004.09.018

Macías, J., Sosa-Ceballos, G., Arce, J., Gardner, J., Saucedo, R., Valdez-Moreno, G. (2017). Storage conditions and magma processes triggering the 1818 CE Plinian eruption of Volcán de Colima. Journal of Volcanology and Geothermal Research, 340, 117-129.Mader, H.M., Llewellin, E.W., & Mueller, S.P. (2013). The rheology of two-phase magmas: A review and analysis. Journal of Volcanology and Geothermal Research, 257, 135–158, doi:10.1016/j.jvolgeores.2013.02.014.

Manga, M., Castro, J., Cashman, K. V., & Loewenberg, M. (1998). Rheology of bubble-bearing magmas. Journal of Volcanology and Geothermal Research, 87(1-4), 15-28.

Martel, C., Andújar, J., Mothes, P., Scaillet, B., Pichavant, M., & Molina, I. (2018). Storage conditions of the mafic and silicic magmas at Cotopaxi, Ecuador. Journal of Volcanology and Geothermal Research, 354, 74-86.

Martin, R.S., Watt, S.F.L., Pyle, D.M., Mather, T.A., Matthews, N.E., Georg, R.B., Day, J.A., Fairhead, T., Witt, M.L.I., & Quayle, B.M. (2009). Environmental effects of ashfall in Argentina from the 2008 Chaitén volcanic eruption. Journal of Volcanology and Geothermal Research, 184(3-4), 462-472.

Mastin, L. G., Guffanti, M., Servranckx, R., Webley, P., Barsotti, S., Dean, K., ... & Waythomas, C. F. (2009). A multidisciplinary effort to assign realistic source parameters to models of volcanic ash-cloud transport and dispersion during eruptions. Journal of Volcanology and Geothermal Research, 186(1-2), 10-21.

Mazzocchi, M., Hansstein, F., & Ragona, M. (2010). The 2010 Volcanic Ash Cloud and Its Financial Impact on the European Airline Industry, CESifoForum, ISSN 2190-717X, ifo Institut für Wirtschaftsforschung an der Universität München, München, Vol. 11, Iss. 2, pp. 92-100.

McCausland, W.A., Pallister, J.S., Andreastutti, S., Gunawan, H., Hendrasto, M., Kasbani, Iguchi, M., & Nakada, S. (2019). Lessons learned from the recent eruptions of Sinabung and Kelud Volcanoes, Indonesia. Journal of Volcanology and Geothermal Research Special Issue.

McPhie, J., Walker, G. P., & Christiansen, R. L. (1990). Phreatomagmatic and phreatic fall and surge deposits from explosions at Kilauea volcano, Hawaii, 1790 AD: Keanakakoi Ash Member. Bulletin of Volcanology, 52(5), 334-354.

Melnik, O., Barmin, A. A., & Sparks, R. S. J. (2005). Dynamics of magma flow inside volcanic conduits with bubble overpressure buildup and gas loss through permeable magma. Journal of Volcanology and Geothermal Research, 143(1-3), 53-68.

Miller, C., Mullineaux, D., & Hall, M. (1978). Reconnais-sance Map of Potential Volcanic Hazard from Cotopaxi Volcano, Ecuador: U.S. Geological Survey Miscella-neous Investigation Map I-1702, scale 1:50 000.

Moitra, P., & Gonnermann, H. M. (2015). Effects of crystal shape-and size-modality on magma rheology. Geochemistry, Geophysics, Geosystems, 16(1), 1-26.

Moitra, P., Gonnermann, H.M., Houghton, B.F., & Giachetti, T. (2013). Relating vesicle shapes in pyroclasts to eruption styles. Bulletin of Volcanology, 75:691, doi:10.1007/s00445-013-0691-8

Moitra, P., Gonnermann, H. M., Houghton, B. F., & Tiwary, C. S. (2018). Fragmentation and Plinian eruption of crystallizing basaltic magma. Earth and Planetary Science Letters, 500, 97-104.

Mothes, P. (1992). Lahars of Cotopaxi volcano, Ecuador: Hazard and risk evaluation, in McCall, G., Laming, D., and Scott, S., eds., Geohazards, Natural and Man-Made: London, Chapman and Hall, p. 53–64.

Mothes, P. A., & Hall, M. L. (2008). The plinian fallout associated with Quilotoa's 800 yr BP eruption, Ecuadorian Andes. Journal of Volcanology and Geothermal Research, 176(1), 56-69.

Mueller, S., Scheu, B., Spieler, O., & Dingwell, D. B. (2008). Permeability control on magma fragmentation. Geology, 36(5), 399-402.

Pardo, N., Cronin, S. J., Palmer, A. S., & Németh, K. (2012). Reconstructing the largest explosive eruptions of Mt. Ruapehu, New Zealand: lithostratigraphic tools to understand subplinian–plinian eruptions at andesitic volcanoes. Bulletin of Volcanology, 74(3), 617-640.

Papale, P. (1999). Strain-induced magma fragmentation in explosive eruptions. Nature, 397(6718), 425-428.

Perez, W., Freundt, A., Kutterolf, S., & Schmincke, H. U. (2009). The Masaya Triple Layer: a 2100 year old basaltic multi-episodic Plinian eruption from the Masaya Caldera Complex (Nicaragua). Journal of Volcanology and Geothermal Research, 179(3-4), 191-205.

Pistolesi, M., Rosi, M., Cioni, R., Cashman, K.V., Rossotti, A., & Aguilera, E. (2011). Physical volcanology of the post-twelfth-century activity at Cotopaxi volcano, Ecuador: behavior of an andesitic central volcano. Geol. Soc. Am. Bull. 123, 1193–1215. http://dx.doi.org/10.1130/B30301.1.

Polacci, M., Papale, P., & Rosi, M. (2001). Textural heterogeneities in pumices from the climactic eruption of Mount Pinatubo, 15 June 1991, and implications for magma ascent dynamics. Bulletin of Volcanology, 63(2-3), 83-97.

Proussevitch, A. A., Sahagian, D. L., & Tsentalovich, E. P. (2007). Statistical analysis of bubble and crystal size distributions: Formulations and procedures. Journal of Volcanology and Geothermal Research, 164(3), 95-111.

Pyle, D.M. (1989). The thickness, volume and grainsize of tephra fall deposits. Bulletin of Volcanology, 51(1), 1-15.

Reiss, W. (1874). Uber Lavastrome der Tungurahua und Cotopaxi: Zeitschrift der Deutschen Geologischen Gesellschaft, v. 26, p. 907–927.

Reiss, W., & Stübel, A. (1869–1902). Das Hochgebirge der Republik Ecuador II: Berlin, Petrographische Untersu-chungen des Ostkordillere, 236 p.

Rosi, M., Bertagnini, A., Harris, A. J. L., Pioli, L., Pistolesi, M., & Ripepe, M. (2006). A case history of paroxysmal explosion at Stromboli: timing and dynamics of the April 5, 2003 event. Earth and Planetary Science Letters, 243(3-4), 594-606.

Rossi, E., Bonadonna, C., & Degruyter, W. (2019). A new strategy for the estimation of plume height from clast dispersal in various atmospheric and eruptive conditions. Earth and Planetary Science Letters, 505, 1-12.

Rust, A. C., Manga, M., & Cashman, K. V. (2003). Determining flow type, shear rate and shear stress in magmas from bubble shapes and orientations. Journal of Volcanology and Geothermal Research, 122(1-2), 111-132.

Rust, A. C., & Cashman, K. V. (2011). Permeability controls on expansion and size distributions of pyroclasts. Journal of Geophysical Research: Solid Earth, 116(B11).

Saalfeld, M. A., Kelley, D. F., & Panter, K. S. (2019). Insight on magma evolution and storage through the recent eruptive history of Cotopaxi Volcano, Ecuador. Journal of South American Earth Sciences, 93, 85-101.

Sahagian, D. L., & Proussevitch, A. A. (1998). 3D particle size distributions from 2D observations: stereology for natural applications. Journal of Volcanology and Geothermal Research, 84(3-4), 173-196.

Saucedo, R., Macías, J.L., Gavilanes, J.C., Arce, J.L., & al. (2010). Eyewitness, stratigraphy, chemistry, and eruptive dynamics of the 1913 Plinian eruption of Volcán de Colima, México. Journal of Volcanology and Geothermal Research, 191, 149-166.

Schipper, C. I., Castro, J. M., Tuffen, H., James, M. R., & How, P. (2013). Shallow vent architecture during hybrid explosive–effusive activity at Cordón Caulle (Chile, 2011–12): evidence from direct observations and pyroclast textures. Journal of Volcanology and Geothermal Research, 262, 25-37.

Schneider, C. A., Rasband, W. S., & Eliceiri, K. W. (2012). NIH Image to ImageJ: 25 years of image analysis. Nature methods, 9(7), 671-675.

Scollo, S., Del Carlo, P., & Coltelli, M. (2007). Tephra fallout of 2001 Etna flank eruption: Analysis of the deposit and plume dispersion. Journal of Volcanology and Geothermal Research, 160(1-2), 147-164.

Shea, T., Houghton, B. F., Gurioli, L., Cashman, K. V., Hammer, J. E., & Hobden, B. J. (2010). Textural studies of vesicles in volcanic rocks: an integrated methodology. Journal of Volcanology and Geothermal Research, 190(3-4), 271-289.

Shea, T., & Hammer, J. E. (2013). Kinetics of cooling- and decompression-induced crystallization in hydrous mafic-intermediate magmas. Journal of Volcanology and Geothermal Research, 260, 127–145. https://doi.org/10.1016/j.jvolgeores.2013

Smith, P. M., & Asimow, P. D. (2005). Adiabat_1ph: A new public front-end to the MELTS, pMELTS, and pHMELTS models. Geochemistry, Geophysics, Geosystems, 6(2).

Smyth, M.A., & Clapperton, C.M. (1986). Late Quater-nary volcanic debris avalanche at Cotopaxi, Ecuador: Revista Centro Interandino Americano de Fotointer-pretación CIAF (Bogotá), v. 11, p. 24–38.

Sodiro, L. (1877). Relación Sobre la Erupción del Cotopaxi Acaecida el Día 26 de Junio de 1877: Quito, Imprenta Nacional, 40 p.

Sparks, R. S. J. (1978). The dynamics of bubble formation and growth in magmas: a review and analysis. Journal of Volcanology and Geothermal Research, 3(1-2), 1-37.

Sparks, R. S. J. (1986). The dimensions and dynamics of volcanic eruption columns. Bulletin of Volcanology, 48(1), 3-15.

Spieler, O., Kennedy, B., Kueppers, U., Dingwell, D. B., Scheu, B., & Taddeucci, J. (2004). The fragmentation threshold of pyroclastic rocks. Earth and Planetary Science Letters, 226(1-2), 139-148.

Stevenson, R. J., Dingwell, D. B., Webb, S. L., & Sharp, T. G. (1996). Viscosity of microlite-bearing rhyolitic obsidians: an experimental study. Bulletin of Volcanology, 58(4), 298-309.

Stübel, A. (1897). Die Vulkanberge Ecuadors: Berlin, A. Asher, 79 p.

Taddeucci, J., Cimarelli, C., Alatorre-Ibargüengoitia, M. A., Delgado-Granados, H., Andronico, D., Del Bello, E., ... & Di Stefano, F. (2021). Fracturing and healing of basaltic magmas during explosive volcanic eruptions. Nature Geoscience, 14(4), 248-254.

Toramaru, A. (2006). BND (bubble number density) decompression rate meter for explosive volcanic eruptions. Journal of Volcanology and Geothermal Research, 154(3-4), 303-316.

Torres-Orozco, R., Cronin, S.J., Pardo, N., Palmer, A.S., 2018. Volcanic hazard scenarios for multiphase andesitic Plinian eruptions from lithostratigraphy: insights into pyroclastic density current diversity at Mount Taranaki, New Zealand. GSA Bull. 130 (9–10), 1645–1663. https://doi.org/10.1130/B31850.1.

Tuffen, H., James, M. R., Castro, J. M., & Schipper, C. I. (2013). Exceptional mobility of an advancing rhyolitic obsidian flow at Cordón Caulle volcano in Chile. Nature Communications, 4(1), 1-7.

Vergniolle, S., & Jaupart, C. (1986). Separated two-phase flow and basaltic eruptions. Journal of Geophysical Research: Solid Earth, 91(B12), 12842-12860.

von Humboldt, A. (1837–1838). Geognostische und physika- lische Beobachtungen uber die Vulkane des Hochlandes von Poggendorffs: Annalen der Physik und Chemie, v. 40, p. 161–193 and v. 44, p. 193–219.

Wadsworth, F., Llewellin, E., Vasseur, J, Gardner, J., & Tuffen, H. (2020). Explosive-effusive volcanic eruption transitions caused by sintering. Sci. Adv. 6:eaba7940.

Walker, G. P., Self, S., & Wilson, L. (1984). Tarawera 1886, New Zealand—a basaltic plinian fissure eruption. Journal of Volcanology and Geothermal Research, 21(1-2), 61-78.

Whymper, E. (1892). Viajes a Través de los Majestuosos Andes del Ecuador: Salt Lake City, Utah, Peregrine Smith Books, 456 p.

Williams, S. N. (1983). Plinian airfall deposits of basaltic composition. Geology, 11(4), 211-214.

Wilson, L., & Walker, G. P. L. (1987). Explosive volcanic eruptions-VI. Ejecta dispersal in plinian eruptions: the control of eruption conditions and atmospheric properties. Geophysical Journal International, 89(2), 657-679.

Wolf, T. (1878). Memoria Sobre el Cotopaxi y su Ultima Erupción Acaecida el 26 de Junio de 1877: Guayaquil, Imprenta de El Comercio, 48 p.

Wolf, T. (1904). Crónica de los Fenómenos Volcánicos y Terremotos en el Ecuador, con Algunas Noticias sobre otros Países de la América Central y Meridional, desde 1533 hasta 1797: Quito, Ecuador, Imprenta de la Universidad Central, 121 p.

Woods, A. W., & Bower, S. M. (1995). The decompression of volcanic jets in a crater volcanic eruptions. Earth and Planetary Science Letters, 131, 189–205.

Zhang, Y. (1999). A criterion for the fragmentation of bubbly magma based on brittle failure theory. Nature, 402(6762), 648-650.

Figures

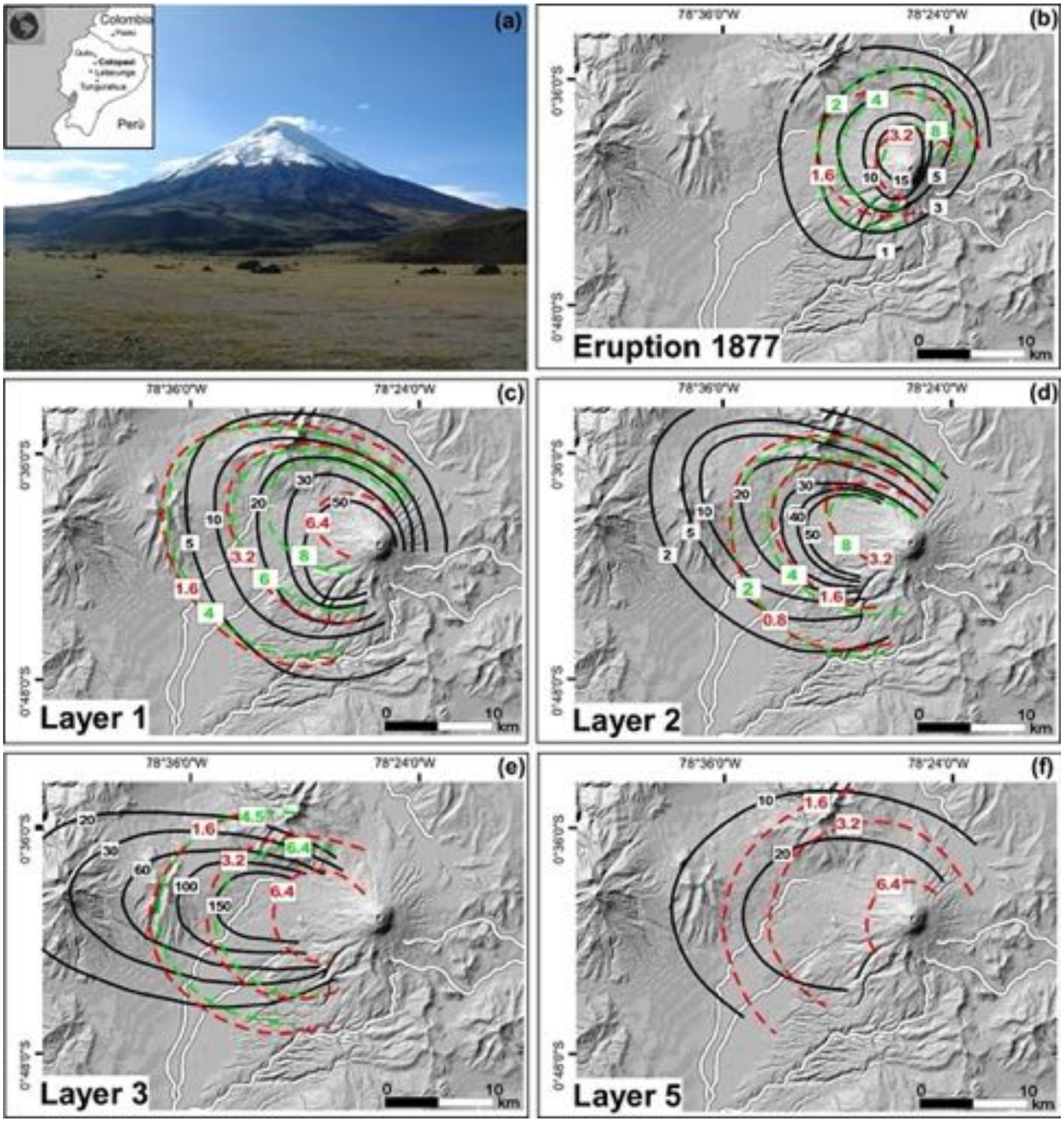

Figure 1. (a) Cotopaxi volcano as seen from the north (localization in the inset). (b-f) Isopach (black lines) contours and isopleth (lithic: red dashed lines; pumice: green dashed lines) contours for the five targeted eruptions of Cotopaxi volcano, whose relief is presented in shaded maps. Data presented here are derived from Barberi et al. (1995), Pistolesi et al. (2011) and Biass and Bonadonna (2011).

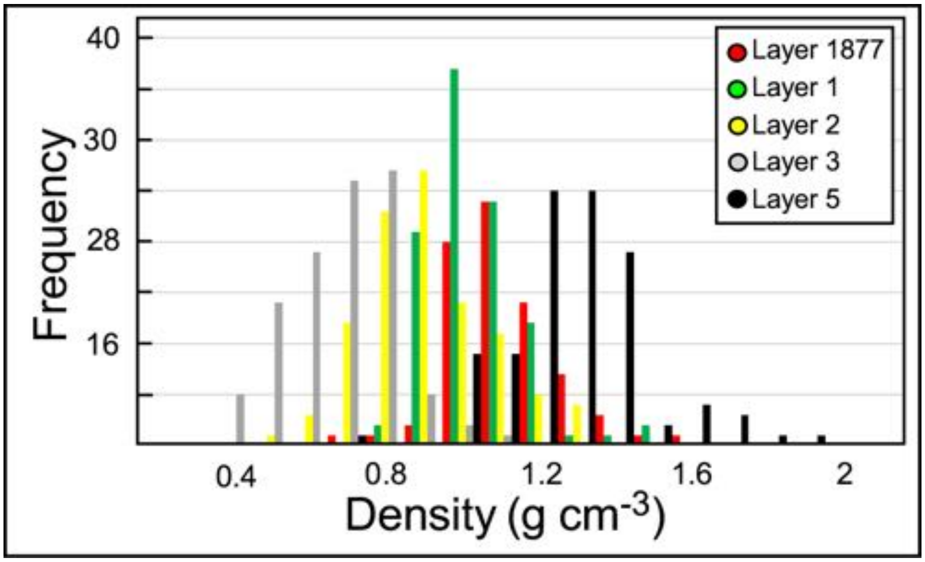

Figure 2. Frequency distributions of bulk density values (gr cm^{-3}) of juvenile fragments for the five selected eruptions (Eruption 1877, and Layers 1, 2, 3 and 5).

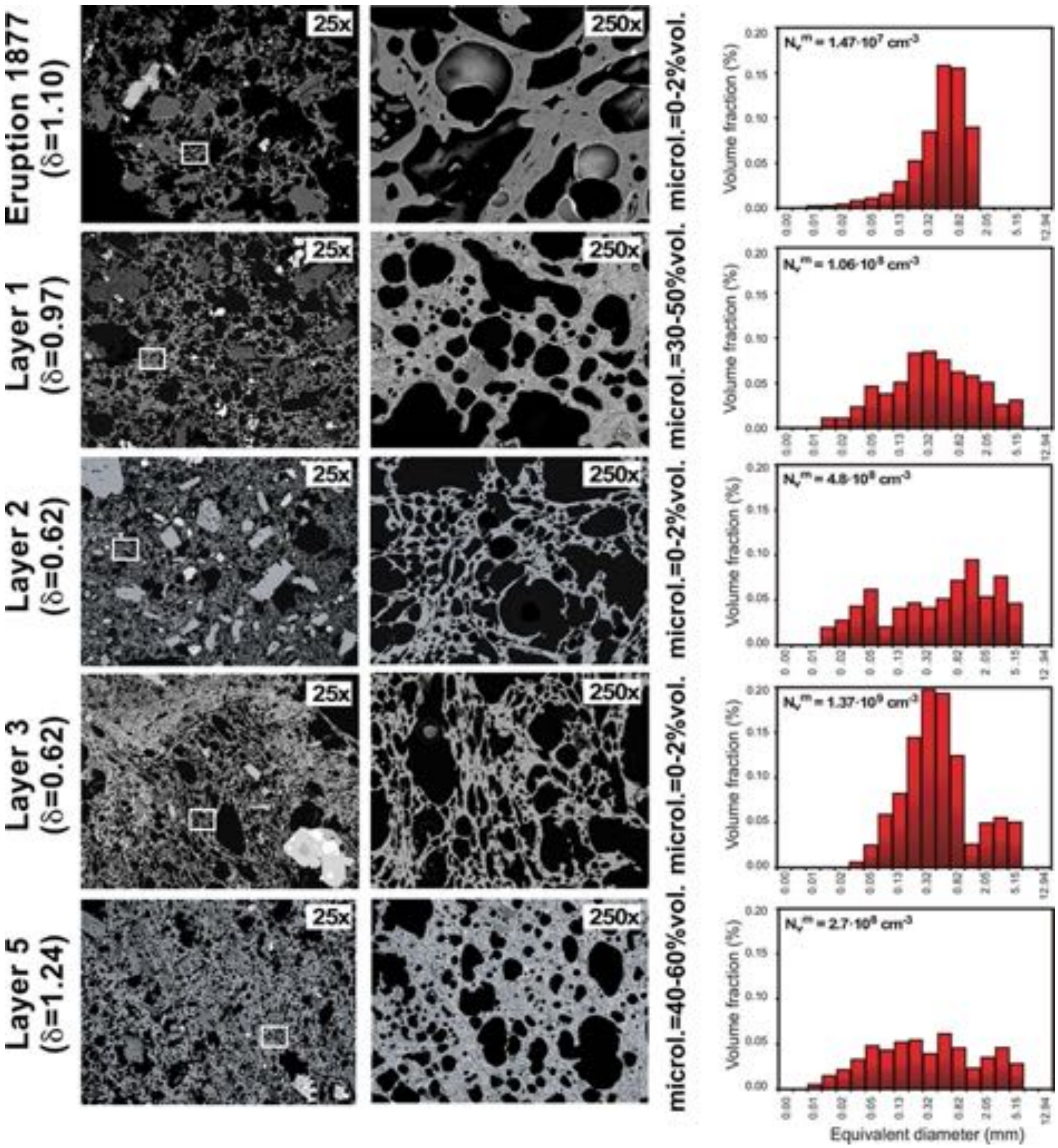

Figure 3. Backscattered Scanning Electron Microscope images of bubble textures and bubble size distribution from Cotopaxi's Eruption 1877, Layer 1, Layer 2, Layer 3 and Layer 5.

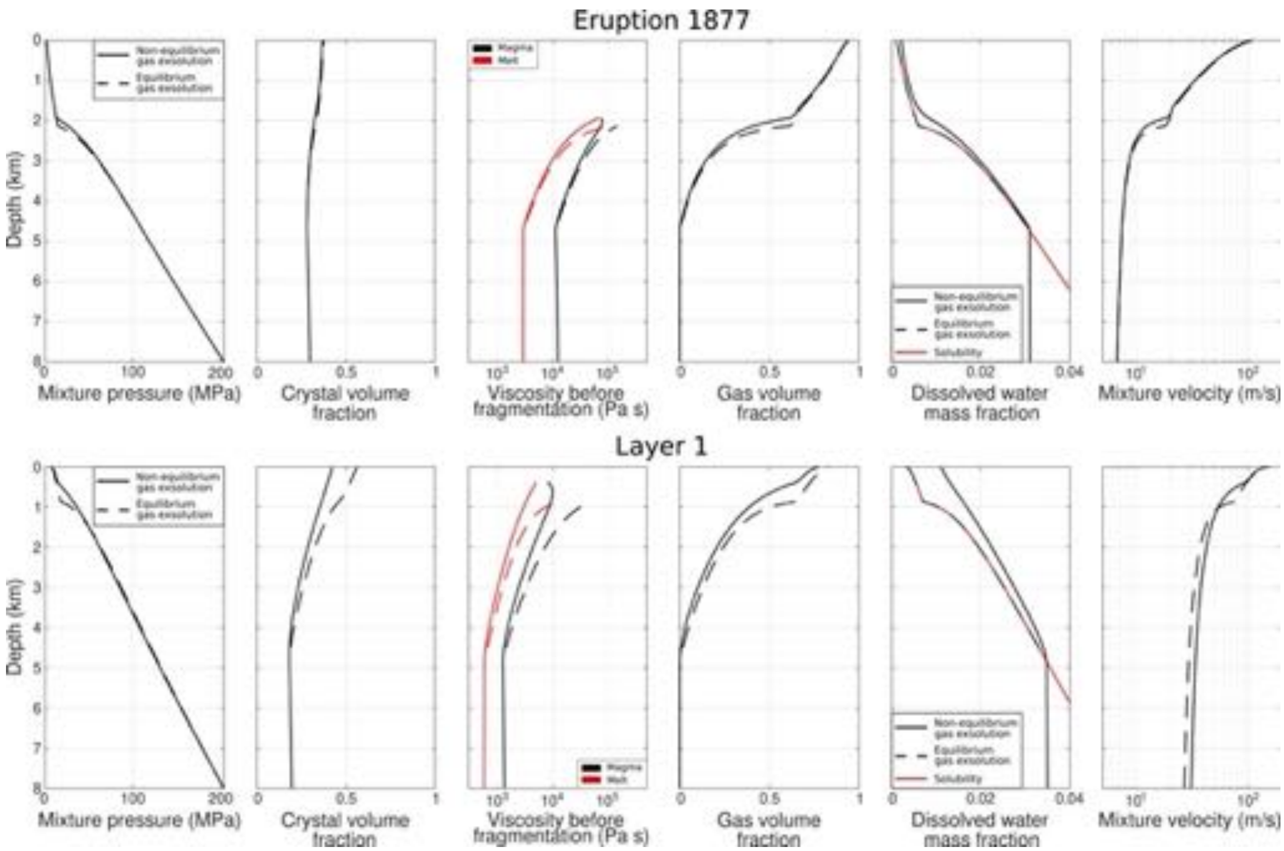

Figure 4. Profiles along the conduit of key physical parameters associated with four specific simulations. Upper panels: Eruption 1877 (equilibrium and non-equilibrium conditions for gas exsolution; water content: 3.1 wt. %; temperature: 950°C). Lower panels: Layer 1 (equilibrium and non-equilibrium conditions for gas exsolution; water content: 3.5 wt. %; temperature: 1000°C). Conduit radius was defined in order to reproduce the computed MER of each eruption (Table 1). Other input parameters are presented in Table 3.

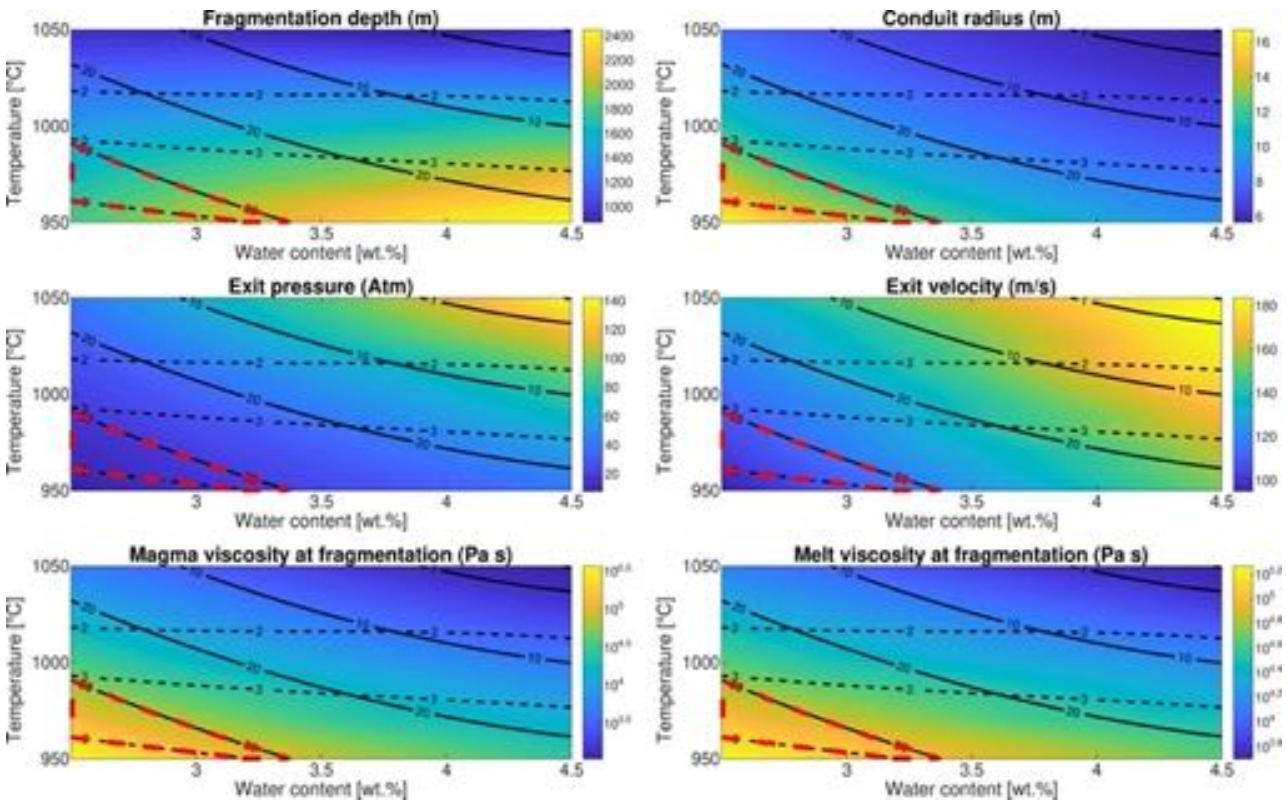

Figure 5. Summary of numerical results associated with Eruption 1877 considering fixed conditions for crystallization and gas exsolution relaxation parameters ($\tau^{(c)} = 1000\ s$ and $\tau^{(d)} = 10^{-4}\ s$). Other inputs are presented in Table 3. Each panel presents a color scale of different output parameters (fragmentation depth, conduit radius, exit pressure, exit velocity, magma viscosity at fragmentation and melt viscosity at fragmentation) as a function of initial temperature and water content. Two superposed contour maps indicate the volume fraction of phenocrysts (continuous lines) and the volume fraction of microlites (dashed lines). The area enclosed by red dashed lines is compatible with our estimates of the volume fraction of microlites and phenocrysts for this eruption, considering a range of tolerance of 5 vol. %.

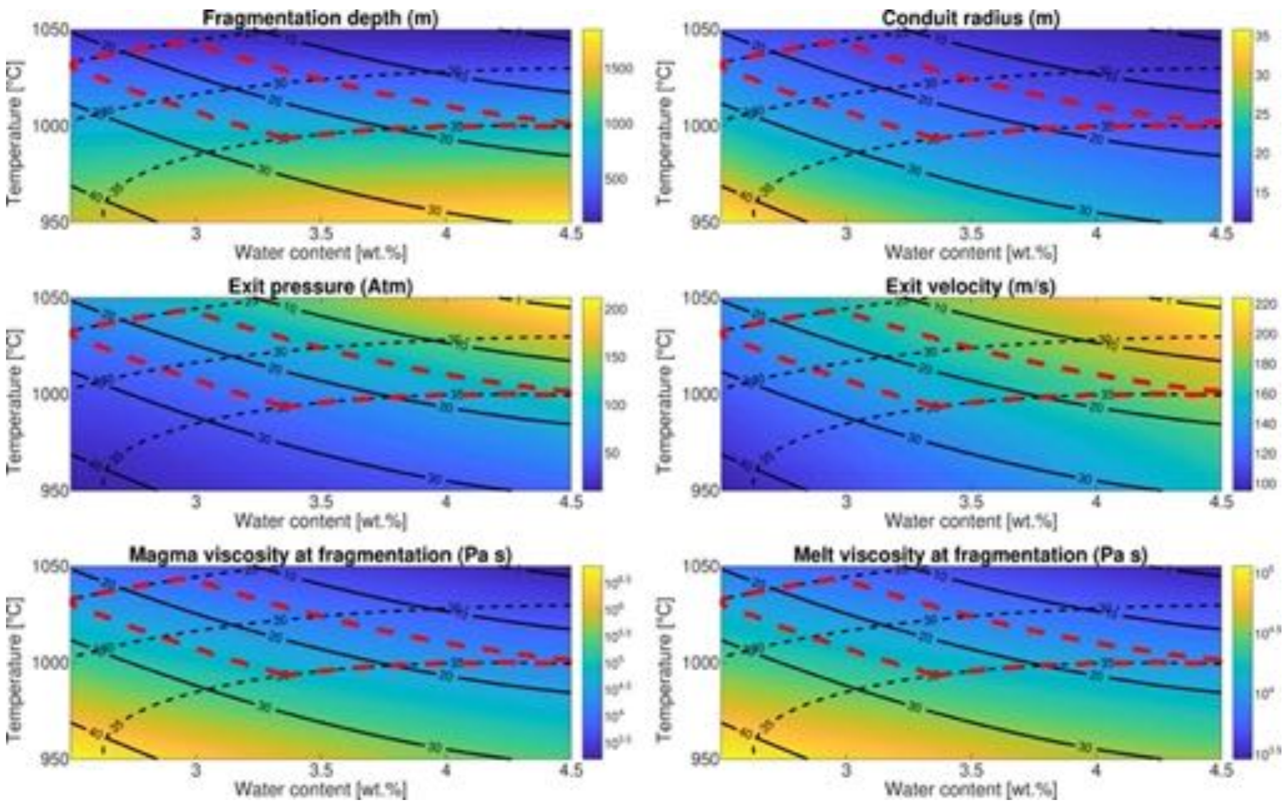

Figure 6. Summary of numerical results associated with Layer 1 considering fixed conditions for crystallization and gas exsolution relaxation parameters ($\tau^{(c)} = 10\ s$ and $\tau^{(d)} = 10^{-4}\ s$). Other inputs are presented in Table 3. Each panel presents a color scale of different output parameters (fragmentation depth, conduit radius, exit pressure, exit velocity, magma viscosity at fragmentation and melt viscosity at fragmentation) as a function of initial temperature and water content. Two superposed contour maps indicate the volume fraction of phenocrysts (continuous lines) and the volume fraction of microlites (dashed lines). The area enclosed by red dashed lines is compatible with our estimates of the volume fraction of microlites and phenocrysts for this eruption, considering a range of tolerance of 5 vol. %.

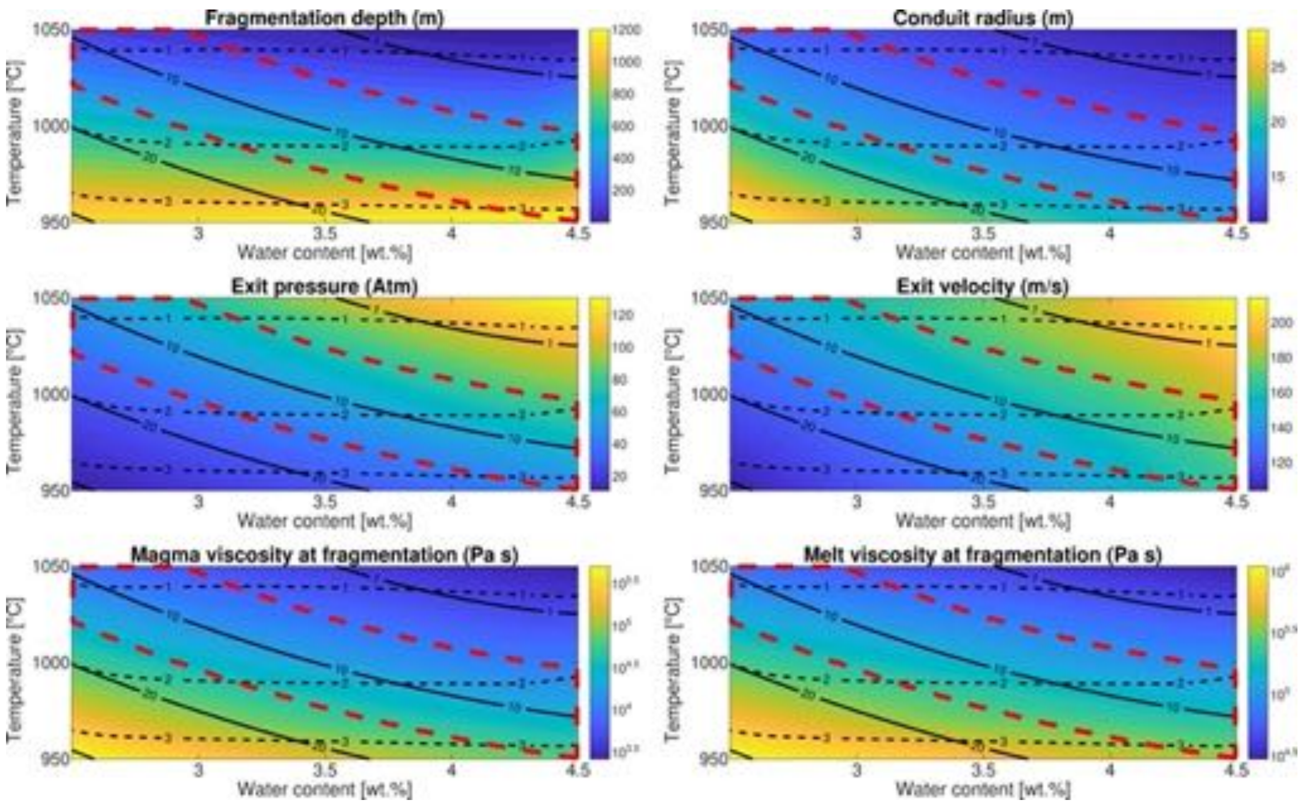

Figure 7. Summary of numerical results associated with Layer 3 considering fixed conditions for crystallization and gas exsolution relaxation parameters ($\tau^{(c)} = 1000\ s$ and $\tau^{(d)} = 10^{-4}\ s$). Other inputs are presented in Table 3. Each panel presents a color scale of different output parameters (fragmentation depth, conduit radius, exit pressure, exit velocity, magma viscosity at fragmentation and melt viscosity at fragmentation) as a function of initial temperature and water content. Two superposed contour maps indicate the volume fraction of phenocrysts (continuous lines) and the volume fraction of microlites (dashed lines). The area enclosed by red dashed lines is compatible with our estimates of the volume fraction of microlites and phenocrysts for this eruption, considering a range of tolerance of 5 vol. %.

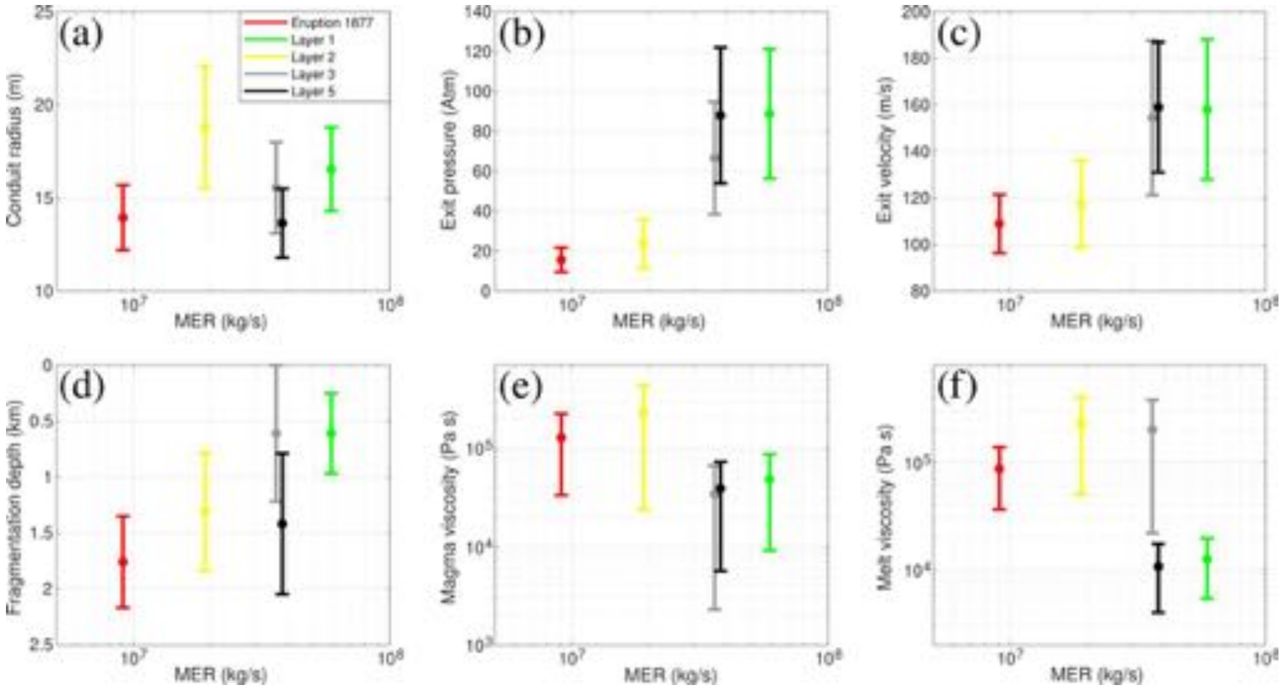

Figure 8. Relationships between MER (calculated from the inversion based on Rossi et al. (2019) and Degruyter and Bonadonna (2012) models; Table 1) of the five selected Cotopaxi eruptions and other key eruption parameters (conduit radius, exit pressure, exit velocity, fragmentation depth, magma viscosity and melt viscosity) derived from conduit modeling. The variability ranges of these parameters were defined considering exclusively the numerical simulations whose results are compatible with textural data (microlites and phenocrysts contents) derived from the studied volcanic products. In other words, we considered the areas enclosed by the red dashed lines in Figures 5-7 and S2-S8.

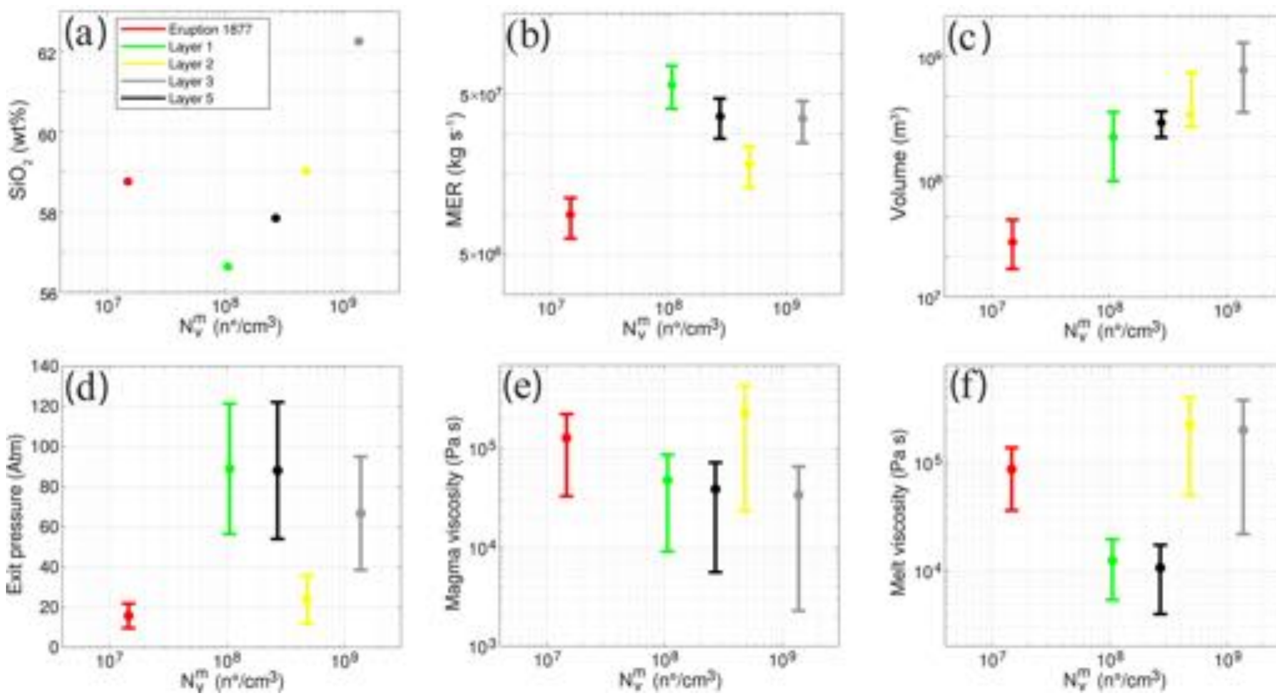

Figure 9. Relationships between Number of vesicles per unit volume (N_v^m, cm^{-3}) of the five selected Cotopaxi eruptions and other key eruption parameters (silica content, MER, volume, exit pressure, magma viscosity and melt viscosity) derived from conduit modeling. MER and volume are calculated from the inversion based on Rossi et al. (2019) and Degruyter and Bonadonna (2012) models, and from the average of Exponential, Power Law and Weibull fits, respectively (see Table 1). The variability ranges of the parameters presented in the lower panels were defined considering exclusively the numerical simulations whose results are compatible with textural data (microlites and phenocrysts contents) derived from the studied volcanic products. In other words, we considered the areas enclosed by the red dashed lines in Figures 5-7 and S2-S8.

Table 1. Eruptive Source Parameters for the five selected eruptions.

Erup./ Layer	Volume (m^3)				Average plume height above vent (km)		Average wind at tropopause (m/s)		Average Mass Eruption Rate – D&B12 (kg/s)		Average Mass Eruption Rate – Ma09 (kg/s)		Average Mass Eruption Rate – W&W87 (kg/s)		Duration (hours)
	Exp.	*PL*	*W*	*Inv.*	*C&S86*	*RBD 19*	*C&S86*	*RBD19*	*C&S86*	*RBD19*	*C&S86*	*RBD19*	*C&S86*	*RBD19*	
1877	2.3×10^{7} [a]	4.9×10^{7} [a]	2.5×10^{7}	-	16.5 [a*]	15.2	6.4 [a*]	4.5	1.5×10^{7}	9.1×10^{6}	1.6×10^{7}	1.1×10^{7}	9.8×10^{6}	7.1×10^{6}	0.5
1	1.4×10^{8} [a]	4.0×10^{8} [a]	1.7×10^{8}	-	25.4 [a*]	20.3	17.5 [a*]	18.7	1.4×10^{8}	5.9×10^{7}	9.5×10^{7}	3.8×10^{7}	5.5×10^{7}	2.2×10^{7}	1.0
2	1.3×10^{8} [a]	8.6×10^{8} [a]	1.2×10^{8}	-	21.4 [a*]	16.1	15.5 [a*]	13.3	6.7×10^{7}	1.9×10^{7}	4.7×10^{7}	1.4×10^{7}	2.8×10^{7}	8.9×10^{6}	3.8
3	6.0×10^{8} [b]	1.5×10^{9} [b]	5.5×10^{8}	2.4×10^{9} [b]	26.8 [b*]	18.1	18.3 [b*]	16.0	1.9×10^{8}	3.6×10^{7}	1.2×10^{8}	2.3×10^{7}	6.8×10^{7}	1.4×10^{7}	4.8
5	2.9×10^{8} [c]	3.8×10^{8} [c]	2.3×10^{8} [c]	5.0×10^{8} [b]	25.6 [b*]	18.7	17.0 [b*]	15.3	1.5×10^{8}	3.8×10^{7}	9.8×10^{7}	2.7×10^{7}	5.7×10^{7}	1.6×10^{7}	2.1

Exp.: Exponential strategy; PL; Power-Law strategy; W: Weibull strategy; Inv.: Inversion Strategy; C&S86: Carey and Sparks (1986); RBD19: Rossi et al. (2019); D&B12: Degruyter and Bonadonna (2012); Ma09: Mastin et al. (2009); W&W87: Wilson and Walker (1987).
All values presented in this table are calculated as part of this work with the exception of: [a], from Pistolesi et al. (2011); [b], from Biass and Bonadonna (2011); [c], from Biass et al. (2019). The values presented with the symbol "*" indicate that the CW and DW ranges have been calculated from the corresponding paper, but the plume height was calculated with the Matlab script of Biass et al. (2015).
Italic values in the exponential column for the calculation of volume indicates values derived with the method of Fierstein and Nathenson (1992) for two segments. All the other values are calculated with the method of Pyle (1989) for one exponential segment.
Heights and winds at the tropopause calculated with C&S86 and RBD19 are averaged over all lithic contours associated with the average of the 3 axes of the 5 largest clasts (3.2 cm and 1.6 cm for Eruption 1877; 6.4 cm, 3.2 cm and 1.6 cm for Layer 1; 3.2 cm, 1.6 cm and 0.8 cm for Layer 2; 3.2 cm, 1.6 cm and 0.8 cm for Layer 3; 6.4 cm, 3.2 cm, 1.6 cm and 0.8 cm for Layer 5).
Height above vent = Height with C&S86 or RBD19 – (Vent height – Sampling height), where Vent height = 5.9 km and Sampling height = 3.0 km.

Parameters used for the calculation of MER with D&B12 equation are: magmatic temperature (1223 K for Layer 3 and 1273 K for Eruption 1877, Layer 1, Layer 2 and Layer 5), tropopause height (17 km), while wind is averaged across plume height.

Table 2. Main physical parameters of tephra samples estimated from textural analyses. Whole-rock and glass matrix data are from Barberi et al. (1995) and from Pistolesi et al. (2011). Mass balance calculations were made with a dedicated spreadsheet using whole rock and groundmass glass analyses from Pistolesi et al. (2011) and mineral data from Saalfeld et al. (2019).

Parameters	Eruption 1877	Layer 1	Layer 2	Layer 3	Layer 5
Average clast density (g/cm^3)	1.10	0.98	0.84	0.62	1.24
Vesicularity derived from density (%)	61.4	65.1	69.7	77.0	54.9
Vesicularity derived from image analysis (%)	38.3	41.4	53.8	57.9	36.6
Microlites content derived from image analysis (vol. %)	0	30	0	0	30
Phenocrysts reanalysed (vol. %)	35	20	30	10	20
Total crystal content derived from mass balance (wt. %)	33	40	35	16	28
Whole-rock SiO_2 (wt. %, normalized)	58.8	56.7	59.1	62.3	57.9
Glass matrix SiO_2 (wt. %)	62.6	59.5	64.4	64.9	60.4
N_A (n°/cm^2)	8.80×10^3	5.13×10^4	2.37×10^5	3.22×10^5	1.24×10^5
N_V (n°/cm^3)	5.56×10^6	3.70×10^7	1.49×10^8	3.15×10^8	1.16×10^8
N_V^m (n°/cm^3)	1.47×10^7	1.06×10^8	4.80×10^8	1.37×10^9	2.70×10^8
Variation range of vesicles diameter (mm)	0.008 – 1.1	0.008 – 6	0.010 – 6	0.008 – 6	0.008 – 6

Table 3. Constitutive equations and main input parameters used in numerical simulations.

Constitutive Equation	**Eruption 1877**	**Layer 1**	**Layer 2**	**Layer 3**	**Layer 5**
Melt viscosity[1]	Giordano et al. (2008)	Giordano et al. (2008)	Giordano et al. (2008)	Giordano et al. (2008)	Giordano et al. (2008)
Effect of bubbles[2]	Costa et al. (2007)	Costa et al. (2007)	Costa et al. (2007)	Costa et al. (2007)	Costa et al. (2007)
Effect of crystals	Costa (2005)	Costa (2005)	Costa (2005)	Costa (2005)	Costa (2005)
Crystallization[3]	alphaMELTS calibration	alphaMELTS calibration	alphaMELTS calibration	alphaMELTS calibration	alphaMELTS calibration
Water solubility[4]	Henry's law	Henry's law	Henry's law	Henry's law	Henry's law
Outgassing[5]	Forchheimer's law	Forchheimer's law	Forchheimer's law	Forchheimer's law	Forchheimer's law
Equations of state (exsolved gas)	Ideal gas	Ideal gas	Ideal gas	Ideal gas	Ideal gas
Equations of state (melt, crystals and pyroclasts)[6]	Mie-Gruneisen equations	Mie-Gruneisen equations	Mie-Gruneisen equations	Mie-Gruneisen equations	Mie-Gruneisen equations
Input parameters	**Eruption 1877**	**Layer 1**	**Layer 2**	**Layer 3**	**Layer 5**
Inlet pressure (MPa)	203.8	203.8	203.8	203.8	203.8
Conduit length (km)	8.0	8.0	8.0	8.0	8.0
Magma water content (wt. %)	2.5 – 4.5	2.5 – 4.5	2.5 – 4.5	2.5 – 4.5	2.5 – 4.5
Temperature (°C)	950 – 1050	950 - 1050	950 - 1050	950 - 1050	950 - 1050
Relaxation time for crystallization (s)	1000	10	1000	1000	10
Relaxation time for gas exsolution (s)	10^{-4} - 10	10^{-4} - 10	10^{-4} - 10	10^{-4} - 10	10^{-4} - 10
Mass discharge rate (kg/s)	9.1×10^{6}	5.9×10^{7}	1.9×10^{7}	3.6×10^{7}	3.8×10^{7}
Bubble number density (m^{-3})	1.47×10^{13}	1.06×10^{14}	4.80×10^{14}	1.37×10^{15}	2.70×10^{14}
Gas volume fraction for fragmentation[7]	61.4%	65.1%	69.7%	77.0%	54.9%

[1]Computed using literature-derived data of glass composition for each eruption (Costantini, 2010).
[2]Costa et al. (2007) adopted a generalisation of Llewellin and Manga (2005).
[3]For each eruption, a set of alphaMELTS (Smith and Asimow, 2005) simulations was performed, considering literature-derived data to define the magma composition (bulk-rock values; Costantini, 2010) and variable values for water content (w; 0.0 wt. % - 4.5 wt. %), pressure (p; 1 – 4000 bar) and temperature (T; 950ºC – 1050ºC). Equilibrium crystallinity (β_{eq}) was fitted considering the following relationship:
$\beta_{eq} = \max(0, \min(1, a_{T^2} \cdot T^2 + a_T \cdot T + a_{p^2} \cdot p^2 + a_p \cdot p + a_{w^2} \cdot w^2 + a_w \cdot w + a_{pw} \cdot p \cdot w + a_{Tw} \cdot T \cdot w + a_{Tp} \cdot T \cdot p + a_0))$,
where T, p and w are expressed in K, bar and mass fraction, respectively. Fit coefficients for each eruption are presented in Table S2.
[4]Fit derived from water solubility data on andesitic melts (Botcharnikov et al., 2015).
[5]Following Degruyter et al. (2012).
[6]Le Métayer et al. (2005).

[7]Assumed equal to the vesicularity estimates derived from density measurements (Table 2). This is because they are generally more reliable than estimates obtained directly from image analysis because of the uncertainty associated with the use of stereological models.

Table 4. Main results derived from conduit numerical modeling.

Parameter	Eruption 1877	Layer 1	Layer 2	Layer 3	Layer 5
Conduit radius (m)	12 – 16	14 – 19	16 – 22	13 – 18	12 – 16
Fragmentation depth (km)	1.4 – 2.2	0.3 – 1.0	0.8 – 1.8	<1.2	0.8 – 2.1
Exit pressure (Atm)	10 – 20	60 – 120	10 – 40	40 – 100	50 – 120
Exit velocity (m/s)	100 – 120	130 – 190	100 – 140	120 – 190	130 – 190
Magma viscosity at fragmentation level (Pa s)	$3.3\times10^4 – 2.2\times10^5$	$9.1\times10^3 – 8.7\times10^4$	$2.3\times10^4 – 4.4\times10^5$	$2.3\times10^3 – 6.6\times10^4$	$5.6\times10^3 – 7.2\times10^4$
Melt viscosity at fragmentation level (Pa s)	$3.6\times10^4 – 1.4\times10^5$	$5.4\times10^3 – 1.9\times10^4$	$5.0\times10^4 – 4.1\times10^5$	$2.2\times10^4 – 3.8\times10^5$	$4.0\times10^3 – 1.7\times10^4$

Figure 1.

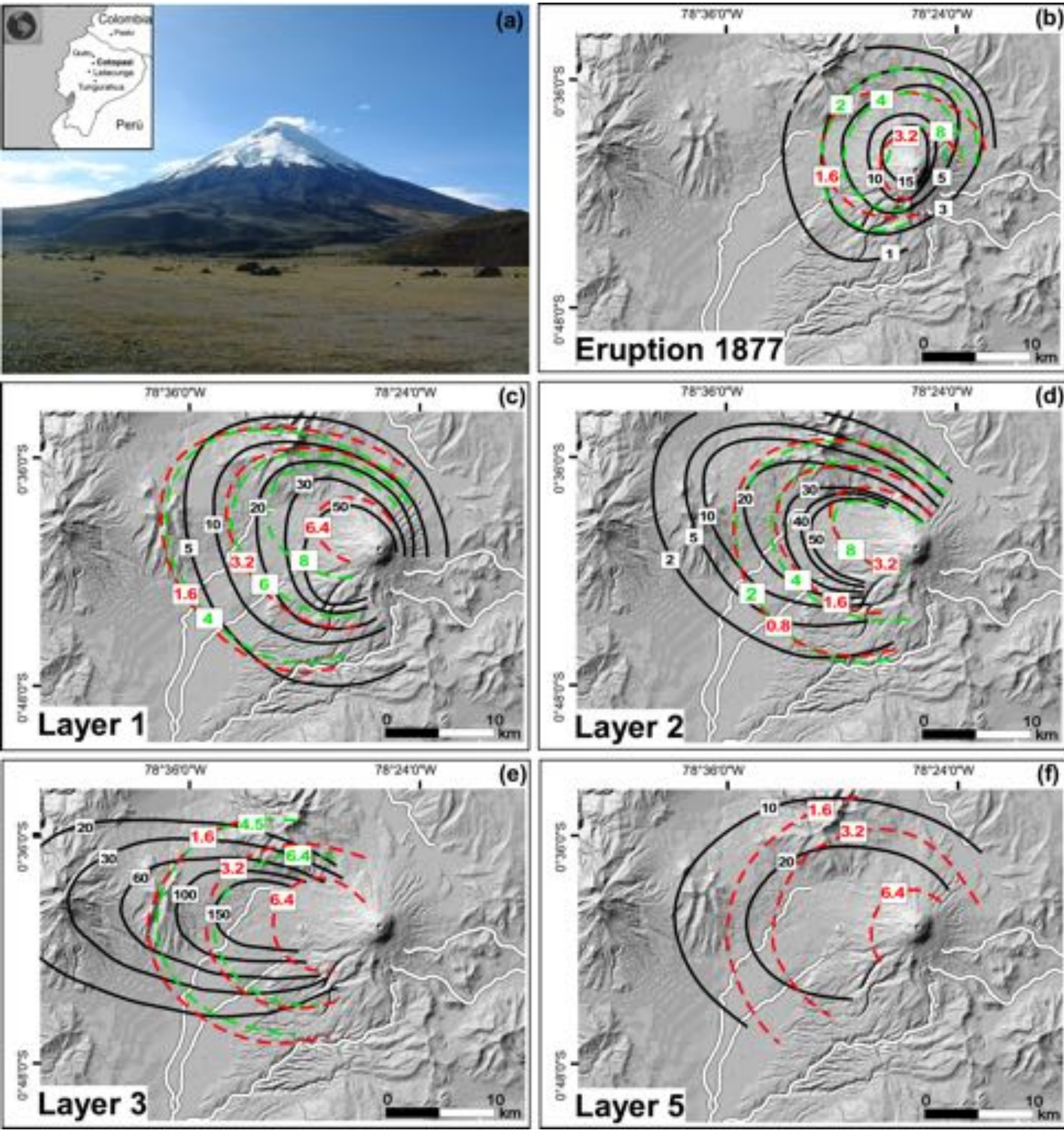
(a)
Colombia
Pasto
Quito
Cotopaxi
Latacunga
Tungurahua
Perú
(b)
78°36'0"W
78°24'0"W
0°36'0"S
0°48'0"S
Eruption 1877
0
5
10
km
(c)
Layer 1
(d)
Layer 2
(e)
Layer 3
(f)
Layer 5

Figure 2.

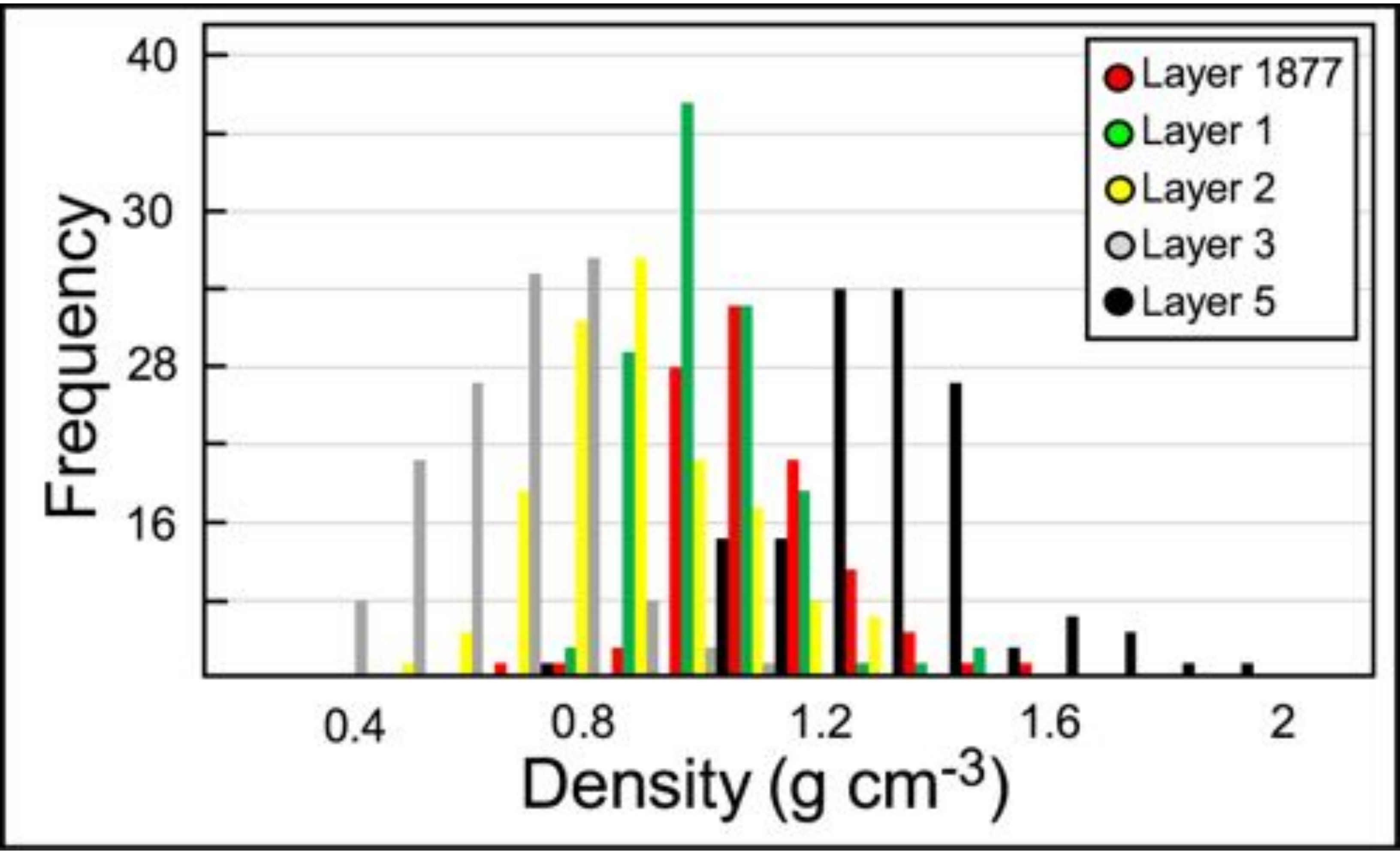
Frequency
40
30
28
16
0.4
0.8
1.2
1.6
2
Density (g cm-3)
Layer 1877
Layer 1
Layer 2
Layer 3
Layer 5

Figure 3.

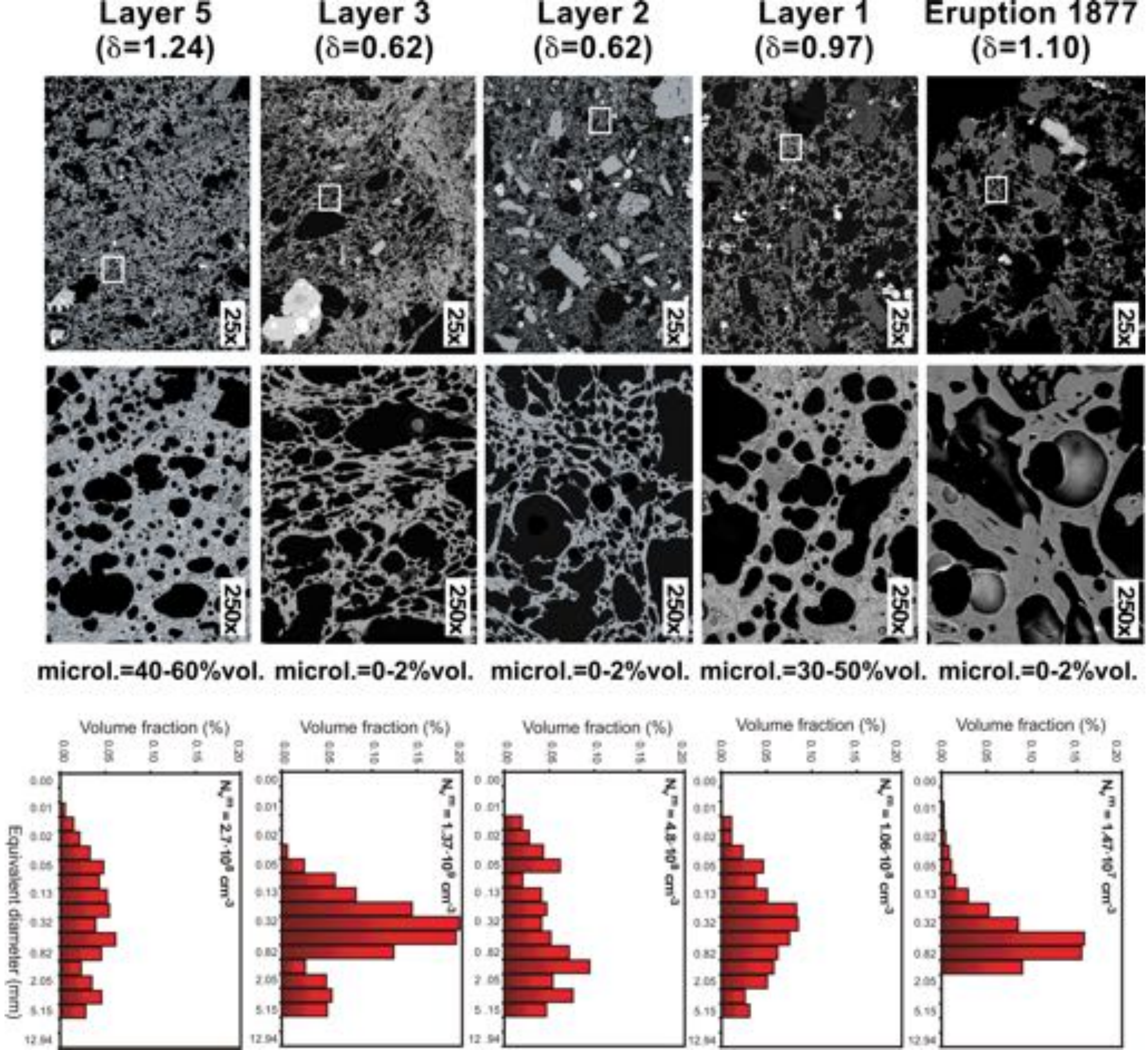

Layer 5 (δ=1.24)
Layer 3 (δ=0.62)
Layer 2 (δ=0.62)
Layer 1 (δ=0.97)
Eruption 1877 (δ=1.10)
25x
250x
microl.=40-60%vol.
microl.=0-2%vol.
microl.=0-2%vol.
microl.=30-50%vol.
microl.=0-2%vol.
$N_v^m = 2.7\cdot10^8$ cm^{-3}
$N_v^m = 1.37\cdot10^9$ cm^{-3}
$N_v^m = 4.8\cdot10^8$ cm^{-3}
$N_v^m = 1.06\cdot10^8$ cm^{-3}
$N_v^m = 1.47\cdot10^7$ cm^{-3}
Volume fraction (%)
Equivalent diameter (mm)

Figure 4.

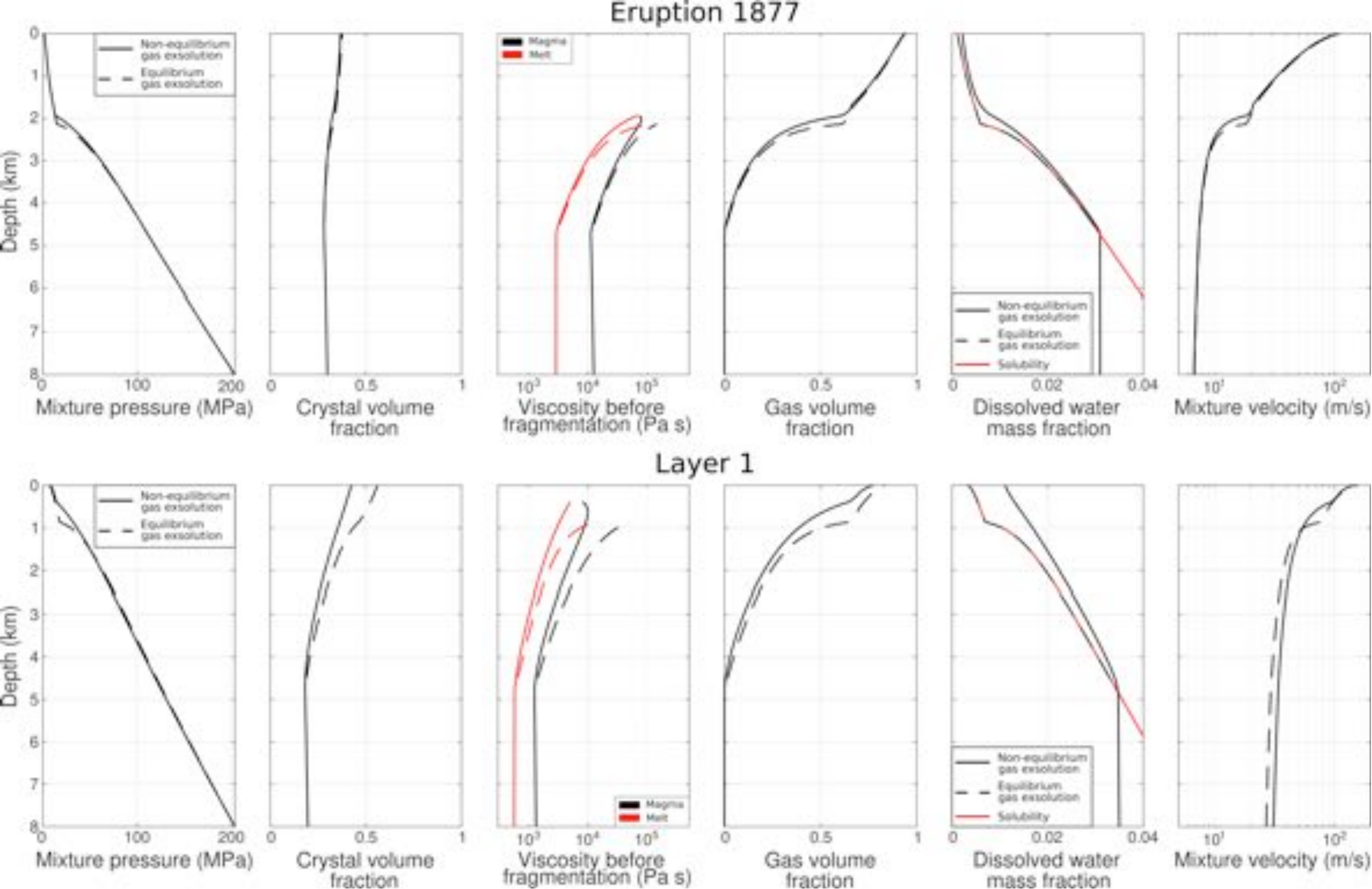

Eruption 1877
Layer 1
Non-equilibrium gas exsolution
Equilibrium gas exsolution
Magma
Melt
Solubility
Depth (km)
Mixture pressure (MPa)
Crystal volume fraction
Viscosity before fragmentation (Pa s)
Gas volume fraction
Dissolved water mass fraction
Mixture velocity (m/s)

Figure 5.

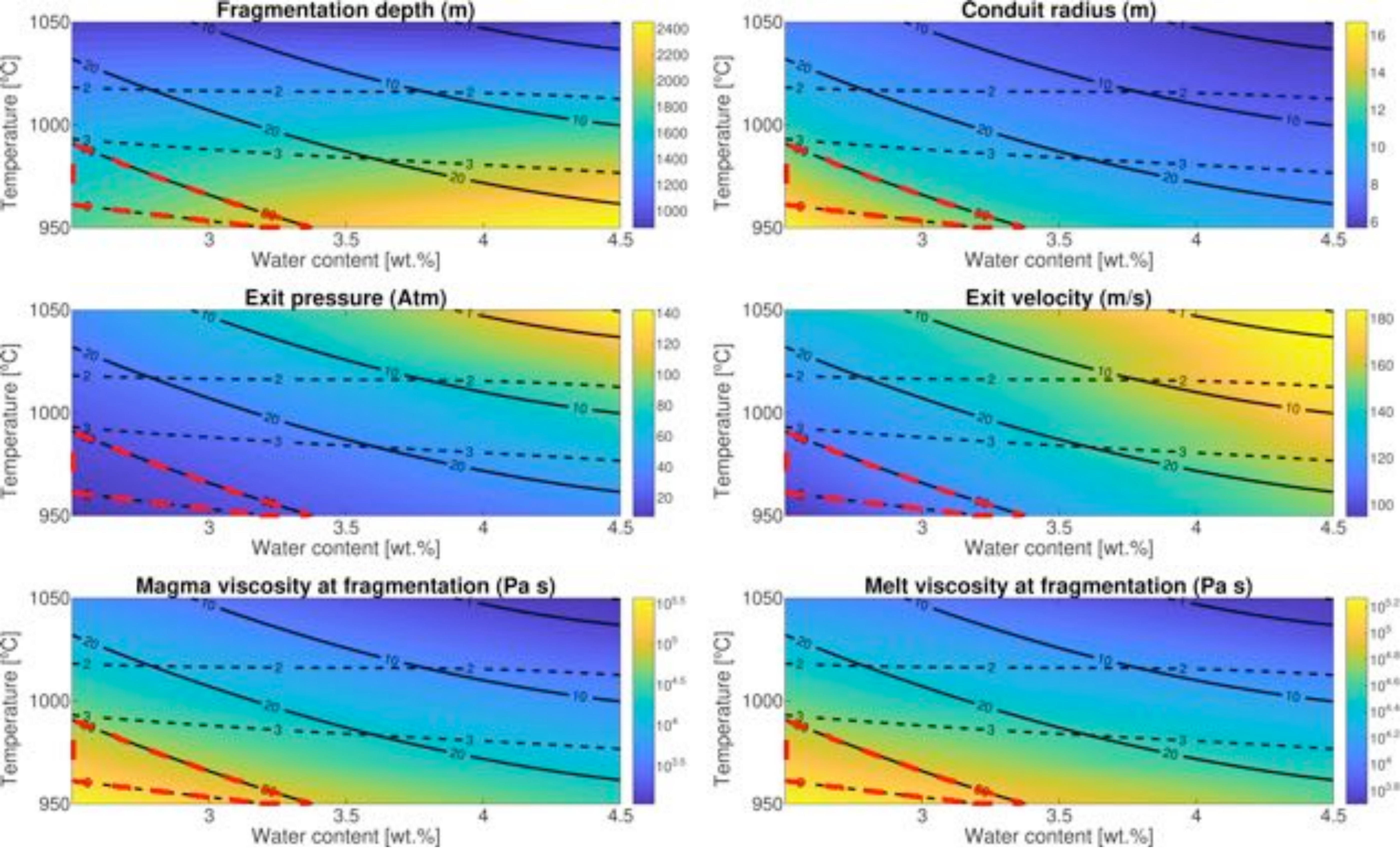

Fragmentation depth (m)
Conduit radius (m)
Exit pressure (Atm)
Exit velocity (m/s)
Magma viscosity at fragmentation (Pa s)
Melt viscosity at fragmentation (Pa s)
Temperature [°C]
Water content [wt.%]

Figure 6.

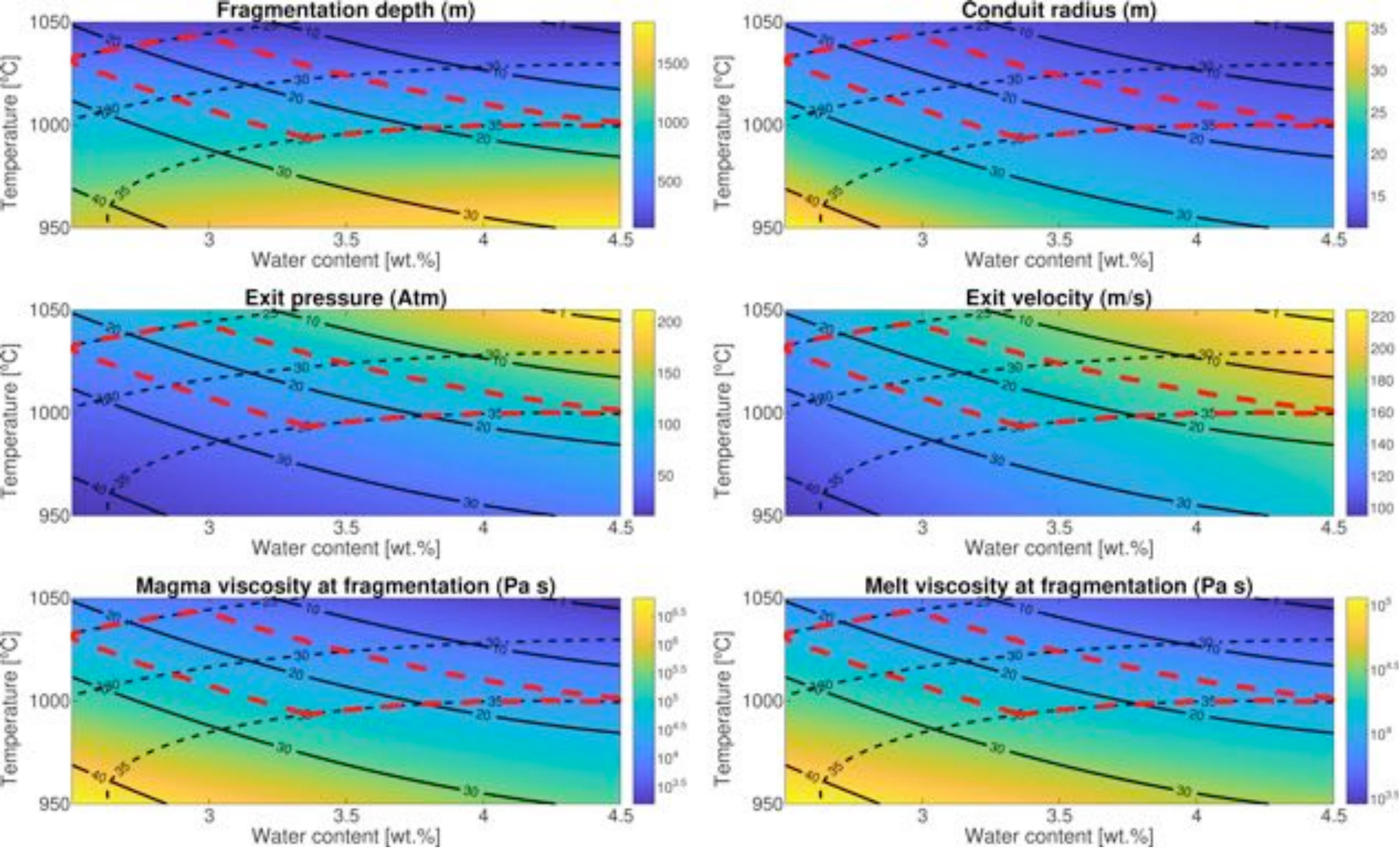

Fragmentation depth (m)
Conduit radius (m)
Exit pressure (Atm)
Exit velocity (m/s)
Magma viscosity at fragmentation (Pa s)
Melt viscosity at fragmentation (Pa s)
Temperature [°C]
Water content [wt.%]

Figure 7.

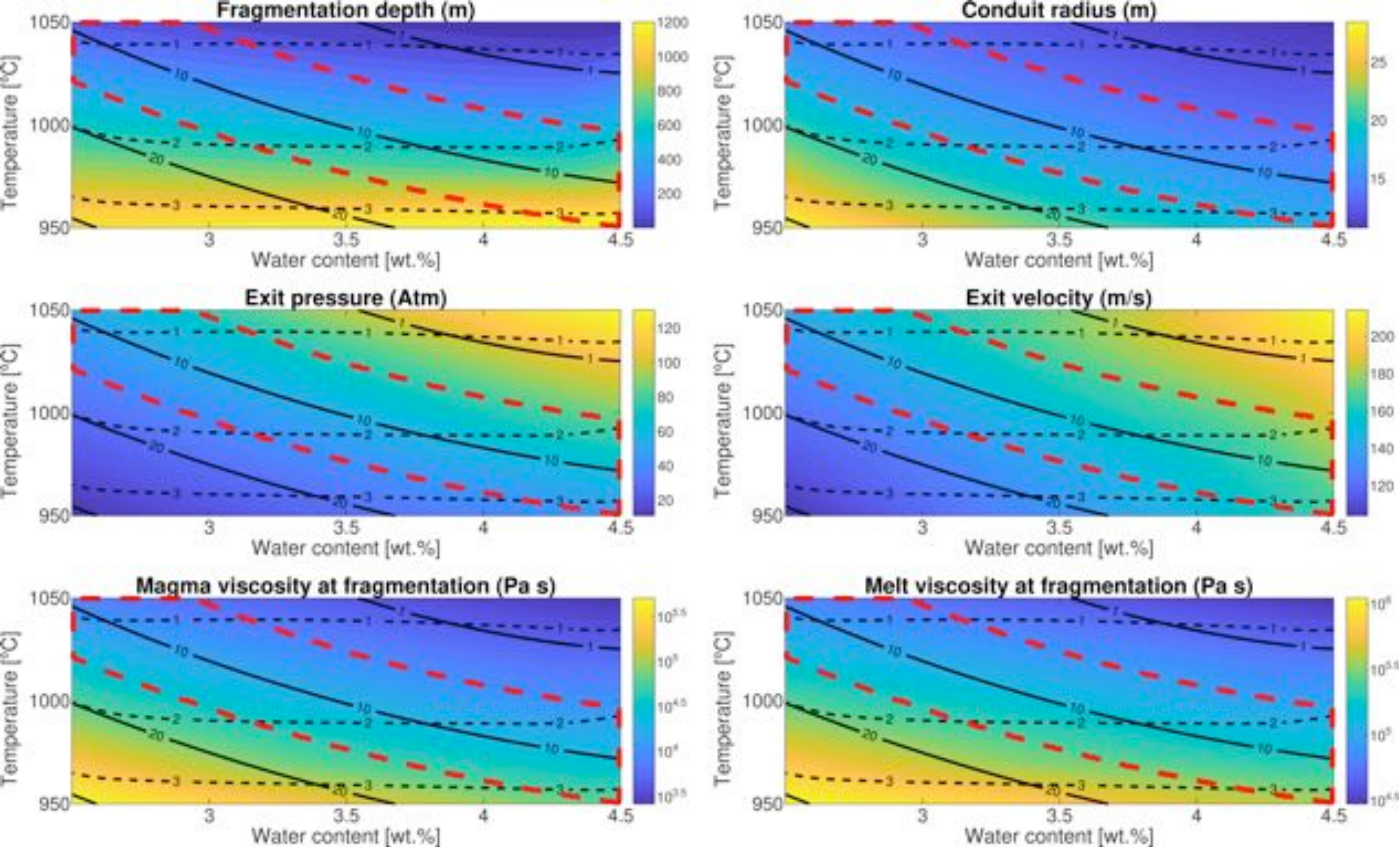

Fragmentation depth (m)
Conduit radius (m)
Exit pressure (Atm)
Exit velocity (m/s)
Magma viscosity at fragmentation (Pa s)
Melt viscosity at fragmentation (Pa s)
Temperature [°C]
Water content [wt.%]

Figure 8.

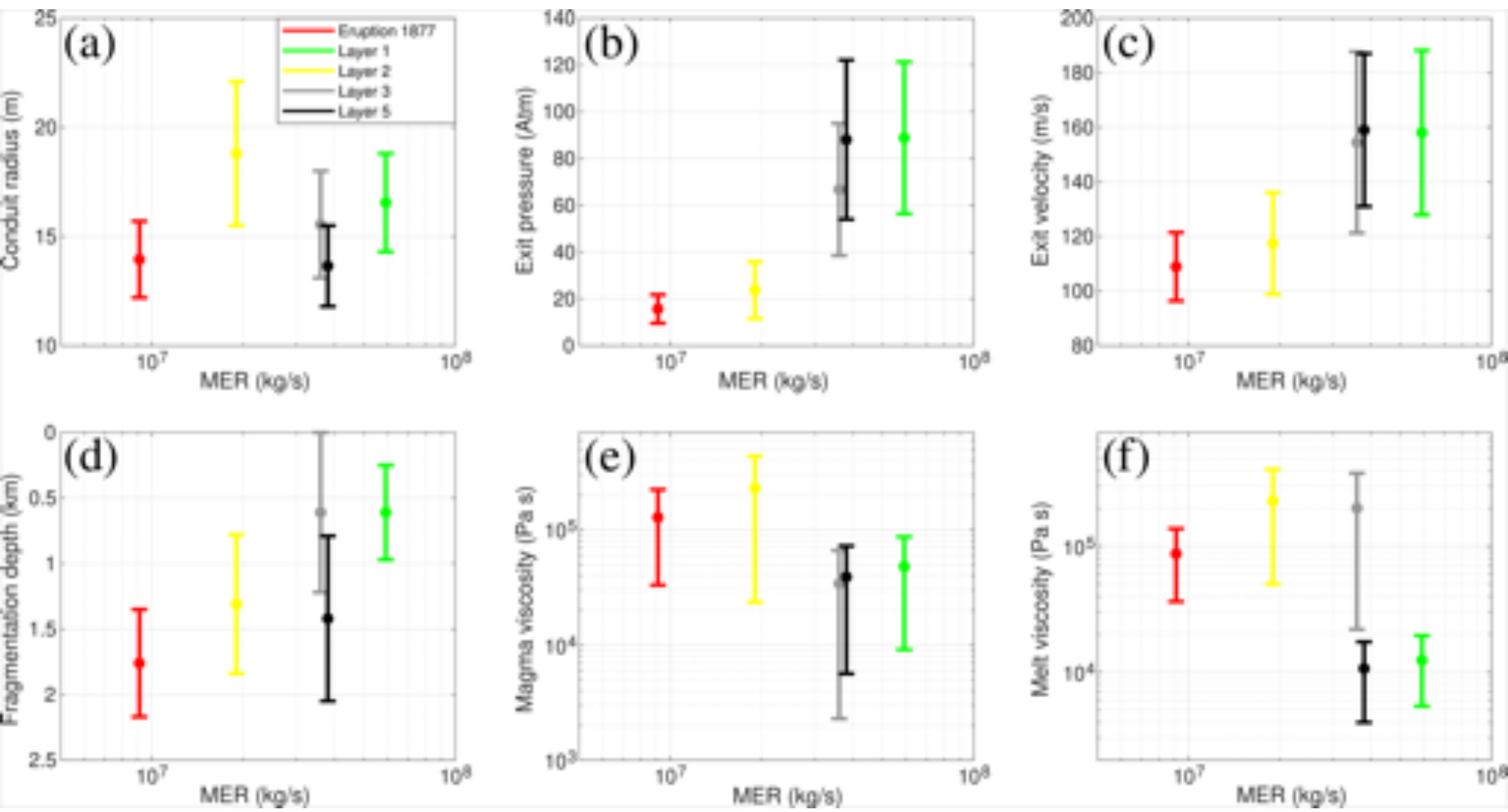

(a)
Eruption 1877
Layer 1
Layer 2
Layer 3
Layer 5
Conduit radius (m)
MER (kg/s)
(b)
Exit pressure (Atm)
MER (kg/s)
(c)
Exit velocity (m/s)
MER (kg/s)
(d)
Fragmentation depth (km)
MER (kg/s)
(e)
Magma viscosity (Pa s)
MER (kg/s)
(f)
Melt viscosity (Pa s)
MER (kg/s)

Figure 9.

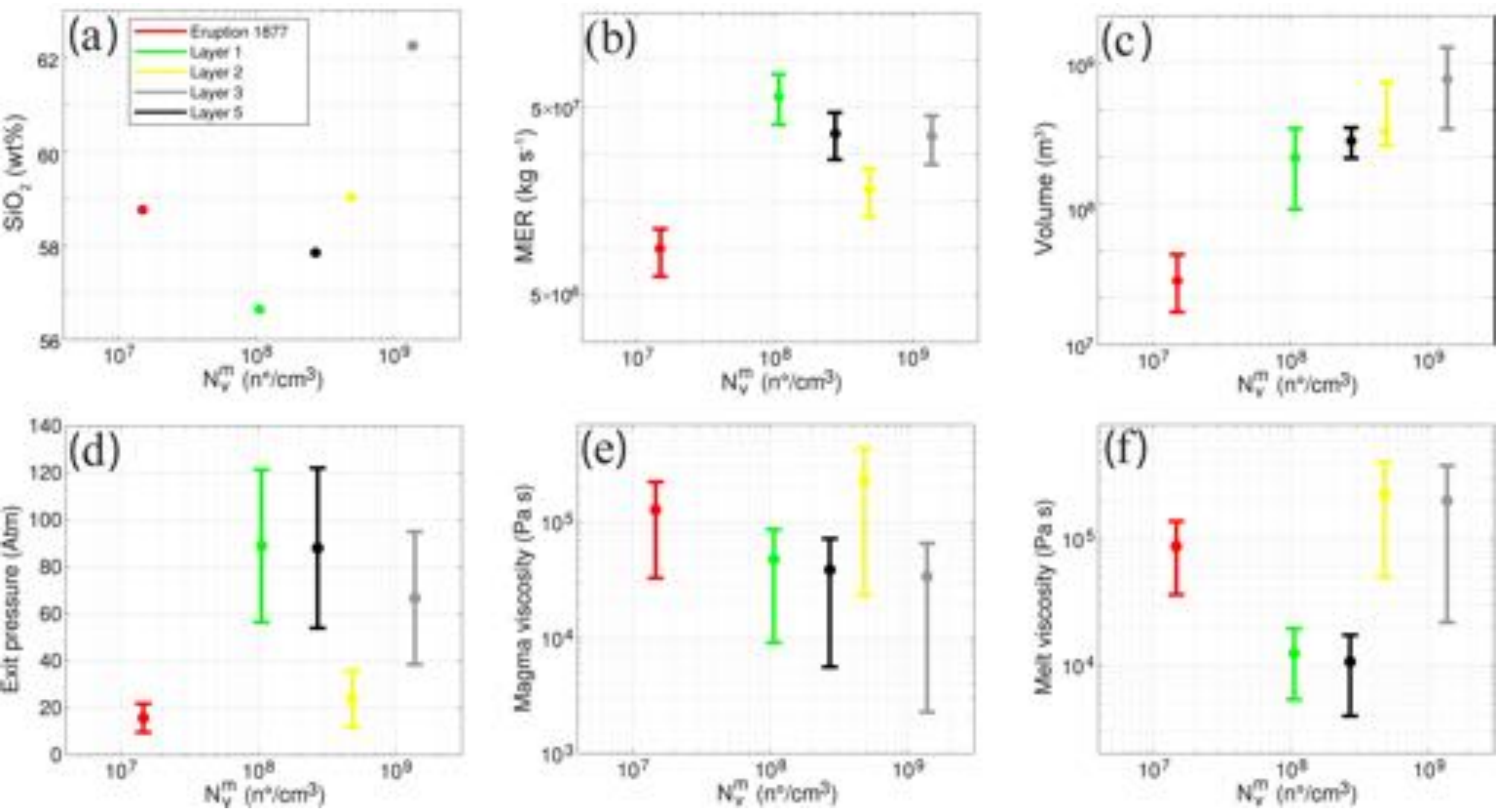

(a)
Eruption 1877
Layer 1
Layer 2
Layer 3
Layer 5
SiO2 (wt%)
(b)
MER (kg s-1)
(c)
Volume (m3)
(d)
Exit pressure (Atm)
(e)
Magma viscosity (Pa s)
(f)
Melt viscosity (Pa s)
Nvm (n°/cm3)

Table 1. Eruptive Source Parameters for the five selected eruptions.

Erup./ Layer	Volume (m^3)				Average plume height above vent (km)		Average wind at tropopause (m/s)		Average Mass Eruption Rate – D&B12 (kg/s)		Average Mass Eruption Rate – Ma09 (kg/s)		Average Mass Eruption Rate – W&W87 (kg/s)		Duration (hours)
	Exp.	*PL*	*W*	*Inv.*	*C&S86*	*RBD 19*	*C&S86*	*RBD19*	*C&S86*	*RBD19*	*C&S86*	*RBD19*	*C&S86*	*RBD19*	
1877	2.3×10^{7} [a]	4.9×10^{7} [a]	2.5×10^{7}	-	16.5[a*]	15.2	6.4[a*]	4.5	1.5×10^{7}	9.1×10^{6}	1.6×10^{7}	1.1×10^{7}	9.8×10^{6}	7.1×10^{6}	0.5
1	1.4×10^{8} [a]	4.0×10^{8} [a]	1.7×10^{8}	-	25.4[a*]	20.3	17.5[a*]	18.7	1.4×10^{8}	5.9×10^{7}	9.5×10^{7}	3.8×10^{7}	5.5×10^{7}	2.2×10^{7}	1.0
2	1.3×10^{8} [a]	8.6×10^{8} [a]	1.2×10^{8}	-	21.4[a*]	16.1	15.5[a*]	13.3	6.7×10^{7}	1.9×10^{7}	4.7×10^{7}	1.4×10^{7}	2.8×10^{7}	8.9×10^{6}	3.8
3	6.0×10^{8} [b]	1.5×10^{9} [b]	5.5×10^{8}	2.4×10^{9} [b]	26.8[b*]	18.1	18.3[b*]	16.0	1.9×10^{8}	3.6×10^{7}	1.2×10^{8}	2.3×10^{7}	6.8×10^{7}	1.4×10^{7}	4.8
5	2.9×10^{8} [c]	3.8×10^{8} [c]	2.3×10^{8} [c]	5.0×10^{8} [b]	25.6[b*]	18.7	17.0[b*]	15.3	1.5×10^{8}	3.8×10^{7}	9.8×10^{7}	2.7×10^{7}	5.7×10^{7}	1.6×10^{7}	2.1

Exp.: Exponential strategy; PL; Power-Law strategy; W: Weibull strategy; Inv.: Inversion Strategy; C&S86: Carey and Sparks (1986); RBD19: Rossi et al. (2019); D&B12: Degruyter and Bonadonna (2012); Ma09: Mastin et al. (2009); W&W87: Wilson and Walker (1987).
All values presented in this table are calculated as part of this work with the exception of: [a], from Pistolesi et al. (2011); [b], from Biass and Bonadonna (2011); [c], from Biass et al. (2019). The values presented with the symbol "*" indicate that the CW and DW ranges have been calculated from the corresponding paper, but the plume height was calculated with the Matlab script of Biass et al. (2015).
Italic values in the exponential column for the calculation of volume indicates values derived with the method of Fierstein and Nathenson (1992) for two segments. All the other values are calculated with the method of Pyle (1989) for one exponential segment.
Heights and winds at the tropopause calculated with C&S86 and RBD19 are averaged over all lithic contours associated with the average of the 3 axes of the 5 largest clasts (3.2 cm and 1.6 cm for Eruption 1877; 6.4 cm, 3.2 cm and 1.6 cm for Layer 1; 3.2 cm, 1.6 cm and 0.8 cm for Layer 2; 3.2 cm, 1.6 cm and 0.8 cm for Layer 3; 6.4 cm, 3.2 cm, 1.6 cm and 0.8 cm for Layer 5).

Height above vent = Height with C&S86 or RBD19 – (Vent height – Sampling height), where Vent height = 5.9 km and Sampling height = 3.0 km.

Parameters used for the calculation of MER with D&B12 equation are: magmatic temperature (1223 K for Layer 3 and 1273 K for Eruption 1877, Layer 1, Layer 2 and Layer 5), tropopause height (17 km), while wind is averaged across plume height.

Table 2. Main physical parameters of tephra samples estimated from textural analyses. Whole-rock and glass matrix data are from Barberi et al. (1995) and from Pistolesi et al. (2011). Mass balance calculations were made with a dedicated spreadsheet using whole rock and groundmass glass analyses from Pistolesi et al. (2011) and mineral data from Saalfeld et al. (2019).

Parameters	Eruption 1877	Layer 1	Layer 2	Layer 3	Layer 5
Average clast density (g/cm^3)	1.10	0.98	0.84	0.62	1.24
Vesicularity derived from density (%)	61.4	65.1	69.7	77.0	54.9
Vesicularity derived from image analysis (%)	38.3	41.4	53.8	57.9	36.6
Microlites content derived from image analysis (vol. %)	0	30	0	0	30
Phenocrysts reanalysed (vol. %)	35	20	30	10	20
Total crystal content derived from mass balance (wt. %)	33	40	35	16	28
Whole-rock SiO_2 (wt. %, normalized)	58.8	56.7	59.1	62.3	57.9
Glass matrix SiO_2 (wt. %)	62.6	59.5	64.4	64.9	60.4
N_A (n°/cm^2)	8.80×10^3	5.13×10^4	2.37×10^5	3.22×10^5	1.24×10^5
N_V (n°/cm^3)	5.56×10^6	3.70×10^7	1.49×10^8	3.15×10^8	1.16×10^8
N_V^m (n°/cm^3)	1.47×10^7	1.06×10^8	4.80×10^8	1.37×10^9	2.70×10^8
Variation range of vesicles diameter (mm)	0.008 – 1.1	0.008 – 6	0.010 – 6	0.008 – 6	0.008 – 6

Table 3. Constitutive equations and main input parameters used in numerical simulations.

Constitutive Equation	Eruption 1877	Layer 1	Layer 2	Layer 3	Layer 5
Melt viscosity[1]	Giordano et al. (2008)	Giordano et al. (2008)	Giordano et al. (2008)	Giordano et al. (2008)	Giordano et al. (2008)
Effect of bubbles[2]	Costa et al. (2007)	Costa et al. (2007)	Costa et al. (2007)	Costa et al. (2007)	Costa et al. (2007)
Effect of crystals	Costa (2005)	Costa (2005)	Costa (2005)	Costa (2005)	Costa (2005)
Crystallization[3]	alphaMELTS calibration	alphaMELTS calibration	alphaMELTS calibration	alphaMELTS calibration	alphaMELTS calibration
Water solubility[4]	Henry's law	Henry's law	Henry's law	Henry's law	Henry's law
Outgassing[5]	Forchheimer's law	Forchheimer's law	Forchheimer's law	Forchheimer's law	Forchheimer's law
Equations of state (exsolved gas)	Ideal gas	Ideal gas	Ideal gas	Ideal gas	Ideal gas
Equations of state (melt, crystals and pyroclasts)[6]	Mie-Gruneisen equations	Mie-Gruneisen equations	Mie-Gruneisen equations	Mie-Gruneisen equations	Mie-Gruneisen equations
Input parameters	**Eruption 1877**	**Layer 1**	**Layer 2**	**Layer 3**	**Layer 5**
Inlet pressure (MPa)	203.8	203.8	203.8	203.8	203.8
Conduit length (km)	8.0	8.0	8.0	8.0	8.0
Magma water content (wt. %)	2.5 – 4.5	2.5 – 4.5	2.5 – 4.5	2.5 – 4.5	2.5 – 4.5
Temperature (°C)	950 – 1050	950 - 1050	950 - 1050	950 - 1050	950 - 1050
Relaxation time for crystallization (s)	1000	10	1000	1000	10
Relaxation time for gas exsolution (s)	10^{-4} - 10	10^{-4} - 10	10^{-4} - 10	10^{-4} - 10	10^{-4} - 10
Mass discharge rate (kg/s)	9.1×10^{6}	5.9×10^{7}	1.9×10^{7}	3.6×10^{7}	3.8×10^{7}
Bubble number density (m^{-3})	1.47×10^{13}	1.06×10^{14}	4.80×10^{14}	1.37×10^{15}	2.70×10^{14}
Gas volume fraction for fragmentation[7]	61.4%	65.1%	69.7%	77.0%	54.9%

[1]Computed using literature-derived data of glass composition for each eruption (Costantini, 2010).
[2]Costa et al. (2007) adopted a generalization of Llewellin and Manga (2005).
[3]For each eruption, a set of alphaMELTS (Smith and Asimow, 2005) simulations was performed, considering literature-derived data to define the magma composition (bulk-rock values; Costantini, 2010) and variable values for water content (w; 0.0 wt. % - 4.5 wt. %), pressure (p; 1 – 4000 bar) and temperature (T; 950ºC – 1050ºC). Equilibrium crystallinity (β_{eq}) was fitted considering the following relationship:
$\beta_{eq} = \max(0, \min(1, a_{T^2} \cdot T^2 + a_T \cdot T + a_{p^2} \cdot p^2 + a_p \cdot p + a_{w^2} \cdot w^2 + a_w \cdot w + a_{pw} \cdot p \cdot w + a_{Tw} \cdot T \cdot w + a_{Tp} \cdot T \cdot p + a_0))$, where T, p and w are expressed in K, bar and mass fraction, respectively. Fit coefficients for each eruption are presented in Table S2.
[4]Fit derived from water solubility data on andesitic melts (Botcharnikov et al., 2015).
[5]Following Degruyter et al. (2012).
[6]Le Métayer et al. (2005).
[7]Assumed equal to the vesicularity estimates derived from density measurements (Table 2). This is because they are generally more reliable than estimates obtained directly from image analysis because of the uncertainty associated with the use of stereological models.

Table 4. Main results derived from conduit numerical modeling.

Parameter	Eruption 1877	Layer 1	Layer 2	Layer 3	Layer 5
Conduit radius (m)	12 – 16	14 – 19	16 – 22	13 – 18	12 – 16
Fragmentation depth (km)	1.4 – 2.2	0.3 – 1.0	0.8 – 1.8	<1.2	0.8 – 2.1
Exit pressure (Atm)	10 – 20	60 – 120	10 – 40	40 – 100	50 – 120
Exit velocity (m/s)	100 – 120	130 – 190	100 – 140	120 – 190	130 – 190
Magma viscosity at fragmentation level (Pa s)	$3.3\times10^{4} – 2.2\times10^{5}$	$9.1\times10^{3} – 8.7\times10^{4}$	$2.3\times10^{4} – 4.4\times10^{5}$	$2.3\times10^{3} – 6.6\times10^{4}$	$5.6\times10^{3} – 7.2\times10^{4}$
Melt viscosity at fragmentation level (Pa s)	$3.6\times10^{4} – 1.4\times10^{5}$	$5.4\times10^{3} – 1.9\times10^{4}$	$5.0\times10^{4} – 4.1\times10^{5}$	$2.2\times10^{4} – 3.8\times10^{5}$	$4.0\times10^{3} – 1.7\times10^{4}$